University of Aveiro Department of Materials and Ceramic Engineering

2013

Sara Isabel

Rodrigues Costa

Ceramic processing and microstructure / property relation in $CaCu_3Ti_4O_{12}$

University of Aveiro

2013

Department of Materials and Ceramic Engineering

Sara Isabel

Rodrigues Costa

Ceramic processing and microstructure / property relation in $CaCu_3Ti_4O_{12}$

Dissertation presented to the University of Aveiro in the fulfillment of the requirement for the awarding of the Masters in Materials Science and Engineering carried out under the supervision of Prof. Jorge Ribeiro Frade, Full Professor in the Department of Materials and Ceramic Engineering at the University of Aveiro, and Prof. Derek Clark Sinclair, Full Professor in the Department of Materials Science and Engineering at the University of Sheffield.

The Board of Examiners

president

Prof**.** Mário Guerreiro Silva Ferreira

Full Professor at the University of Aveiro

Prof. Paula Maria Lousada Silveirinha Vilarinho

Associate Professor at the University of Aveiro

Prof. Manuel Almeida Valente

Asociate Professor at the University of Aveiro

Prof. Jorge Ribeiro Frade (Supervisor)

Full Professor at the University of Aveiro

Prof. Derek Clark Sinclair (Co-supervisor)

Full Professor at the University of Sheffield

Aknowledegments

I would like to thank my supervisors for their guidance and dedication throughout this work, to all people who helped me at the Universities of Aveiro and Sheffield, friends and family.

.

palavras-chave

Condensador, elevada permitividade dielétrica, condensador the interface interna resistiva (IBLC), moagem de alta energia, condutividade elétrica, titanato de cálcio e cobre.

resumo

$CaCu_3Ti_4O_{12}$ (CCTO) foi produzido a temperatura baixa por moagem de alta energia e o seu impacto nas propriedades eléctricas estudado. O CCTO desenvolve um mecanismo de condensador de interface interna resistiva (do inglês IBLC) devido a desvios de estequiometria da composição inicial, a temperaturas de processamento intermédias (900-1100 ^{o}C). Este projeto tem como objectivo diminuir a temperatura de calcinação e, consequentemente, a de sinterização, de forma a reter a composição estequiométrica durante o processamento do CCTO. A evolução da fase CCTO foi controlada por difração de raios-X e as amostras foram sinterizadas pelo método convencional no intervalo de temperaturas entre 700 e 1100 ^{o}C, e caraterizadas por espetroscopia de impedância em temperaturas criogénicas e acima de temperatura ambiente. As amostras sinterizadas a 1100 ^{o}C foram, em seguida, caraterizadas por SEM e EDS.

Os resultados mostram que a técnica de moagem de alta energia permite produzir pós de CCTO a temperaturas mais baixas, 700 ^{o}C, quando comparada com a síntese convencional por reação no estado sólido (950 - 1100 ^{o}C). As medidas por espetroscopia de impedância mostram que as amostras sinterizadas a 700 ^{o}C são constituídas por grãos resistivos com resistividade > 1 MΩ cm a 523 K e, portanto, a composição estequiométrica permanece inalterada e o mecanismo de IBLC não está presente. A densidade relativa é, contudo, bastante baixa, 57 %. Com o aumento da temperatura de sinterização, os grãos começam a tornar-se semicondutores e o mecanismo IBLC começa a desenvolver-se, acompanhado por um decréscimo acentuado da resistividade do grão em pelo menos seis ordens de grandeza. Para temperaturas de sinterização intermédias, 800 - 900 ^{o}C, os grãos são constituídos por uma fase semicondutora rodeada por uma fase resistiva. Para temperaturas de sinterização de 1000 ^{o}C, os grãos são semicondutores com resistividade ~ 40 Ω cm e fronteiras de grão ~ 530 Ω cm a 523 K. As amostras sinterizadas a 1100 ^{o}C são constituídas por grãos semicondutores e fronteiras de grão resistivos com resistividade ~ 65 kΩ cm a 523 K. Esta diferença de resistividades parece estar na origem da elevada permitividade dielétrica no intervalo de radiofrequências.

A análise por EDS revela que a amostra sinterizada a 1100 ^{o}C é deficiente em cobre, o que contribui para o aumento da condutividade do grão. A transformação do grão resistivo em semicondutor parece estar, portanto, associada à difusão e eventual volatilização de cobre a temperaturas de processamento elevadas.

keywords *Capacitor, high dielectric permittivity, Internal Barrier Layer Capacitor (IBLC), high-energy milling, electric conductivity, calcium copper titanate.*

Abstract

$CaCu_3Ti_4O_{12}$ (CCTO) powders were produced at low temperatures by high-energy ball milling and its impact on the electrical properties of CCTO ceramics carried out. CCTO ceramics develop an internal barrier layer capacitance (IBLC) mechanism due to small changes in stoichiometry, which seems to start at intermediate processing temperatures (900 - 1100 ^{o}C). This project aims to decrease the calcination and sintering temperatures to retain the stoichiometric composition during processing of CCTO ceramics. The evolution of the CCTO phase was evaluated by X-ray diffraction and ceramics were prepared by conventional sintering at temperatures between 700 and 1100 ^{o}C. The samples were characterised by impedance spectroscopy at subambient and high temperatures. Ceramics sintered at 1100 ^{o}C were characterised by SEM and EDS.

The results show that high-energy ball milling permits the production of CCTO powder at lower temperature, 700 ^{o}C, compared to conventional solid state reaction (950 - 1100 ^{o}C). Impedance spectroscopy measurements show that ceramics sintered at a temperature of 700 ^{o}C, the stoichiometric composition of CCTO is retained and consists of insulating grains with a resistivity > 1 MΩ cm at 523 K. The relative density is, however, rather low, 57 %, and the IBLC mechanism is not present in this sample as usually observed for CCTO ceramics. When the sintering temperature increases, the insulating grains start to transform into semiconducting and the IBLC mechanism starts to appear, accompanied by a significant drop on the resistivity by at least six orders of magnitude for ceramics sintered at 1000 ^{o}C. At intermediate sintering temperatures, 800 - 900 ^{o}C, the grains are electrically heterogeneous containing both insulating and semiconducting phases. When samples are sintered at 1000 ^{o}C, the grains are totally semiconducting with resistivity of ~ 40 Ω cm and grain boundary resistivity of ~ 530 Ω cm at 523 K. Ceramics sintered at 1100 ^{o}C exhibit semiconducting grains surrounded by insulating grain boundary with resistivity of ~ 65 kΩ cm at 523 K, and this seems to be responsible for the high effective permittivity at radio frequencies for dense ceramics.

The EDS analysis shows CCTO ceramics sintered at 1100 ^{o}C to be Cu-deficient and it contributes to the increase of the bulk conductivity. The transformation of the resistive into semiconducting grains and the evolution of the IBLC mechanism may be, therefore, linked to the diffusion and eventual volatilisation of copper at elevated processing temperatures.

Contents

List of figures

List of tables

List of symbols and Abbreviations

Symbols

a - lattice parameter

A – sample sectional area

C - capacitance

C_b- bulk capacitance

C_{gb} – grain boundary capacitance

d - spacing between planes in the atomic lattice

$d_{theoretical}$ – theoretical density

%d – relative density

E_a –activation energy

f – frequency

I – current intensity

k - Boltzmann constant ($1{,}38 \times 10^{-23}$ J K^{-1})

L – sample thickness

M_A – Atomic mass

M'' – real part of electric modulus

M*- electric modulus

n – Layers index number

N_A – atomic number

r – ionic radii

R – resistivity

R_b – bulk resistivity

R_{gb} – grain boundary resistivity

t – tolerance factor

T_c – curie temperature

t_b – bulk thickness

t_{gb} – grain boundary thickness

T - absolute temperature

V – potential difference

V_{cell} – unit cell volume

Y* - admittance

Z' – real part of impedance

Z'' – imaginary part of impedance

Z – impedance of a circuit element

Z* - impedance

ε_0 - permittivity of vacuum (8.854×10^{-12} F m^{-1})

ε^* - permittivity

ε_{eff} – effective permittivity

ε_r – intrinsic or bulk permittivity

Θ - angle between the incident ray and scattering planes

λ – wavelength

σ - conductivity

σ_0 - pre-exponential factor of conductivity

τ – time constant

Φ_m – work function of the metal

Φ_s – effective work function of the semiconductor

ω – angular frequency

Abbreviations

ac – alternating current

ABX_3 - general formula of a perovskite

BCTO - $Bi_{2/3}Cu_3Ti_4O_{12}$

BEI - backscattered electron image

BLM - Brickwork Layer Model

BT – $BaTiO_3$

CCTO – $CaCu_3Ti_4O_{12}$

CCTO 700 – sample sintered at 700 ^oC

CCTO 800 – sample sintered at 800 ^oC

CCTO 900 – sample sintered at 900 ^oC

CCTO 1000 – sample sintered at 1000 ^oC

CCTO 1100 – sample sintered at 1100 ^oC

CCMTO - $CaCu_{2.94}Mn_{0.06}Ti_4O_{12}$

dc - direct current

DRAM - Dynamic Random Access Memory

EDS - energy-dispersive X-ray spectroscopy

HEBM - high-energy ball milling

IBLC - Internal Barrier Layer Capacitor

IS - impedance spectroscopy

SEM - scanning electron microscopy

ST - $SrTiO_3$

TG - thermogravimetric analysis

XRD - X-ray diffraction

YCTO - $Y_{2/3}Cu_3Ti_4O_{12}$

YSZ - yttria-stabilized zirconia

1. Introduction

Nowadays, a big challenge in the microelectronics industry is to decrease the size of the passive components, especially, the capacitors. Materials with high dielectric constant have been, therefore, the target of attention. Since the discovery of ferroelectricity in single crystals of Rochelle salt in 1921[1], much work has been done to find new materials possessing high dielectric constant. During the World War II, the study of ferroelectrics increased rapidly with the discovery of Barium titanate ($BaTiO_3$). Most materials with high dielectric constant have ferroelectric characteristics such as $BaTiO_3$ [2], a classic material used in the capacitor industry, due to an atomic displacement of Ti^{4+} within the unit cell. These materials possessing ferroelectric characteristics display some disadvantages since the dielectric constant is dependent on the temperature, reaching a maximum at a fixed temperature, known to as the Curie temperature. Above the Curie temperature a phase transition occurs, accompanied by an abrupt decrease on the dielecric permittivity, compromising the use of $BaTiO_3$ for some applications such as capacitores[3]. Therefore, a new class of materials with non-ferroelectric characteristics but exhibiting high dielectric permittivity has been extensively studied in recent years. It is the case of $CaCu_3Ti_4O_{12}$ (CCTO), a non-ferroelectric material, which exhibits a 'giant' dielectric constant of about 10^4 to 10^5 and stable over a wide temperature range from 100 to 600 K.[4,5] However, CCTO exhibits high dielectric losses at high frequencies (> MHz), where the dielectric constant drops down to 100. Due to these characteristics, CCTO can be used in the manufacture of electronic components such as multilayer capacitors, electronic devices such as DRAM and microwave devices.[6,7] There are also other materials that have large dielectric constant and similar electric behaviour as CCTO, such as $Bi_{2/3}Cu_3Ti_4O_{12}$ (BCTO), $Y_{2/3}Cu_3Ti_4O_{12}$ (YCTO), among others.

CCTO has high dielectric constant due to an internal barrier layer capacitance (IBLC) mechanism. This effect, however, is poorly understood, since questions regarding the development of the n-type semiconductivity as well as the effect of processing on the electrical properties of CCTO ceramics are still unclear. Changing the synthesis technique in the preparation of CCTO powder with high purity may be helpful to the understanding of the effect of processing on the final electrical properties of CCTO ceramics.

In this work, CCTO powders were produced by a different synthesis method, high-energy ball milling, in order to decrease the calcination and sintering temperatures and study the effect on the electrical properties of ceramics by impedance spectroscopy (IS).

1.1. Perovskite compounds

There is a wide variety of compounds that have the perovskite structure due to its flexibility to accommodate almost all elements in the periodic table. Most of them are oxides and fluorides and can be composed from many combinations of anions and cations. This diversity results in a broad range of physical properties (dielectric, magnetic, optical, etc) and, therefore, different technological applications. For example, $BaTiO_3$ is a ferroelectric material with high dielectric constant near its Curie temperature and hence, an important material in the capacitor industry. $Ba(Bi_{1-x}Pb_x)O_3$ is used for the production of superconductors, $La_{1-x}Ca_xMnO_3$ is a material which displays magnetoresistive and magnetostrictive properties and so on.[8] For these reasons, perovskite structured compounds have been extensively studied for many years.

1.2. Perovskite structure

The general formula for a perovskite compound is ABX_3 in which F^-, Cl^- and O^{2-} can be incorporated into the structure in the X position [9]. The perovskite structure can be divided in two main groups: the ideal cubic perovskite and distorted cubic perovskite which corresponds to most of ABX_3 compounds.[10,11]

1.2.1. Ideal cubic perovskite structure

The ideal cubic perovskite structure belongs to the cubic space group Pm3m, with coordination number of six and twelve for the B and A cations, respectively. X anion is coordinated by two B cations and four A cations. An example of a compound with an ideal perovskite structure is strontium titanate, $SrTiO_3$.[8,10,11]

The most common description for the structure consists of a three-dimensional cubic network of corner-sharing MX_6 octahedra, where the A cation is in the center of a cube defined by eight corner-sharing octahedral units with B in the center of each one. Note that all B-X-B and O-X-O

angles are 180 and 90°, respectively. Figure 1.1 illustrates the structure of a perovskite with the description just mentioned.[10]

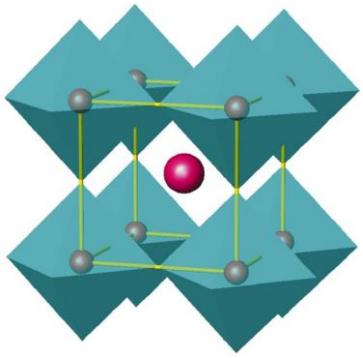

Figure 1.1 – Schematic of the Pm3m perovskite structure including an outline of the cubic unit cell. The BX_6 units are represented as octahedra with B atoms visible within them, and the A ion centrally located in the cube-octahedral cavity between the octahedra.[10]

Most perovskite compounds, however, do not exhibit the ideal structure just described, but instead they are distorted, usually, accompanied by loss of symmetry, which significantly affects the physical properties. The type of distortion is important to understand the relation between the crystal structure and physical properties of a material.

1.2.2. Structural distortions on perovskites

There are essentially three factors identified so far as contributing to the perovskite distortion: size effects, deviations from the ideal composition and Jahn-Teller effects. These effects usually act simultaneously in the distortion of the ideal cube.[9]

1.2.2.1. Size effects

In the ideal cube the cell axis, a, is geometrically related to the ionic radii (r_A, r_B and r_O) according to the equation: [9,12,13]

$$a = \sqrt{2}(r_A + r_O) = 2(r_B + r_O) \quad (1)$$

The ratio of the two expressions for the cell length is called the Goldschmidt's *tolerance factor t* and is a "measure" of the degree of distortion of a perovskite, described as follow:

$$t = \frac{(r_A + r_O)}{\sqrt{2}(r_B + r_O)} \quad (2)$$

The distortion happens when the A cation is too small and is not in contact with the anions anymore. As a consequence the B-X-B bond bends slightly, tilting the BX_6 octahedra in order to keep the contact between anions and A cations. $SrTiO_3$, an ideal perovskite, assumes naturally *t*=1,00 with r_A=1,44 Å, r_B=0,605 Å and r_O=1,40 Å. If the A ion is smaller than the ideal value then t becomes smaller than 1. The cubic structure, however, remains if 0,89 < t < 1. For smaller values the structure loses the symmetry. $GdFeO_3$, for example, has t < 1 and the structure is orthorhombic with r_A=1,107 Å and r_B=0,78 Å. For t < 0,8, the stable structure is ilmenite. The tolerance factor can be more than 1 if the A cation is too large or the B cation too small and the structure is hexagonal.[9]

1.2.2.2. Deviation from the ideal ABX_3 composition

Deviation from the ideal ABX_3 composition occurs by having vacant sites which would normally be occupied or the cations have different valency. This is the case for $SrFeO_y$ (2,5 ≤ y ≤ 3) where the valency of Fe changes as it is heated in an oxidizing or reducing atmosphere. When y < 3, $SrFeO_x$ is composed of a mixture of Fe^{3+} and Fe^{4+} ions. This is a common example of a defect perovskite in which deviations from the ideal composition results in distorted perovskites.[9]

The existence of tetragonal, orthorhombic, rhombohedral, monoclinic and triclinic perovskites arises, therefore, on the deviations from the ideal structure. In most cases, the substitution occurs on the cation sites leading to a large class of compounds with the general formula $AA'BB'X_6$. Such substitutions can be made either in a random or ordered way. Usually the symmetry of ordered perovskites is compromised and might lead, in many cases, to a change of the unit cell length.[8]

1.2.3. Distortion of the ideal cubic perovskite

The ideal perovksite structure can be distorted by three different mechanisms occurring separately or in combination: distortions of octahedra, cation displacements within octahedra and tilting of octahedra. The first two distortion mechanisms are due to electronic instabilities of the octahedral metal ion. For example, the ferroelectric $BaTiO_3$ displays an electronic instability that leads to cation displacement of Ti^{4+} from the centre of the octahedron. Basically, cation displacement is the movement of one or both A and B-site cations within the structure from their respective symmetry sites, causing what is called ferroelectricity.[8]

Octahedral distortion involves no ion displacement, but instead, changes in the shape of the octahedra by increasing or decreasing B-O bond length.

Octahedral tilting is the most common distortion in perovskites, representing 80 - 90 % of all perovskites and is described in more detailed in the next section.[14]

1.2.3.1. Tilting of octahedra

As mentioned before, tilting of octahedra is seen in almost all perovskites and it occurs when the A-site cation is too small for the cubic BX_3 corner-sharing octahedral network. This distortion consists of the tilting of BX_6 about one or more of its symmetry axes and involves only the soft B-X-B bond angle. Octahedral tilting usually does not change the coordination of the A cation, however, there are four Glazer tilt systems that are an exception to this rule: $a^+a^+a^+$, $a^+a^+c^-$, $a^0b^+b^+$ and $a^0b^+b^-$, with the most important one being $a^+a^+a^+$ tilting. The $a^+a^+a^+$ tilt system is usually present in perovskites with general formula of $AA'_3B_4X_{12}$ and alters the coordination environment of the A-site cation, leading to a four-coordinate square planar environment for A' with short A'-X bonds and a 12- coordinate icosahedral environment for A.[3,8,10,14,15]

Associated with $a^+a^+a^+$ tilting is therefore an introduction of cation ordering and to date there are approximately 40 $AA'_3B_4X_{12}$ perovskites in which ordering of the A and A' cations is stabilized by $a^+a^+a^+$ tilting. A corresponds to the larger cation and A' to the smaller cation, for example, Cu^{2+} and Mn^{3+}, respectively. The combination of octahedra tilting with cation ordering usually doubles the length of the unit cell so changing the space group symmetry of the material.[8,14]

1.2.4. Double perovskites

As mentioned in the section before, the combined effect of cation ordering and octahedral tilting results in a double unit cell along the three crystallographic directions, to maintain the translational symmetry. As a consequence, the space group of symmetry changes and in most situations results in a loss of symmetry.[8]

Figure 1.2 illustrates the transition of a double unit cell from the simple cube to the ordered and asymmetric body-centered tetragonal cell.

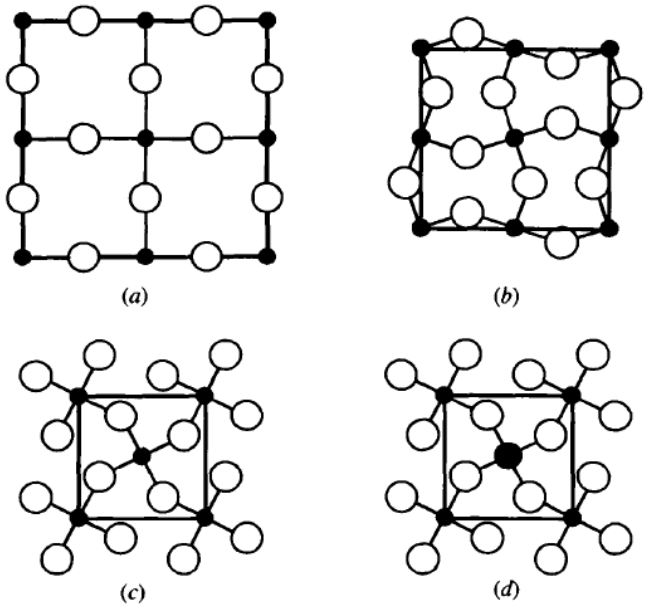

Figure 1.2 - Illustration of a transition from a simple cube to the ordered and asymmetric body-centered tetragonal unit cell.[8]

(a) illustrates an ideal cubic perovskite ABX_3 before octahedral tilting; in (b) the face centered tetragonal cell after an octahedral tilting distortion; in (c) the body-centered tetragonal cell and (d) the ordered body-centered tetragonal cell, where the symmetry has been lost.[8]

To know how the octahedron tilts is fundamental to correlate with the electrical properties of perovskite materials. A notation to characterise the tilting was developed by Glazer.

1.2.5. Glazer notation

Glazer described the octahedral tilting of different perovskite compounds, in 1972, giving rise to 23 different tilt (Glazer) systems. It consists of specifying the rotation of each axis of all three cartesian axes by using two parameters ($a^{\#}b^{\#}c^{\#}$). The letters correspond to the magnitude of the rotation around the [100], [010] and [001] directions of the Pm3m cubic perovskite and the superscript # indicates if two adjacent octahedra rotate in the same or opposite direction and it takes values of *0*, *+* or -. *0* means there is no rotation about the axis, *+* indicates that adjacent octahedra rotates in the same direction and - in the opposite direction.[8,16] The most simple tilt system is that of the ideal cubic perovskite Pm3m described previously; tilt system symbol is $a^0a^0a^0$, that is, there is no rotation around any axis.[8,16]

1.3. $ACu_3Ti_4O_{12}$ compounds

The $ACu_3Ti_4O_{12}$ family of compounds has been known since 1967 and structural described in 1979. The dielectric properties of these compounds, however, were not studied before 2000. Since then, attention has been paid to these compounds due to the high dielectric constant found in most of them, especially $CaCu_3Ti_4O_{12}$, which exhibits the highest value, as shown in table 1.[17] Loss tangent is also provided in table 1.

Table 1 – Relative dielectric constant and loss tangent for $ACu_3B_4O_{12}$ compounds, at 100 kHz (25 ^oC).[17]

Compound	Relative dielectic constant	loss tangent
$CaCu_3Ti_4O_{12}$	10286	0,067
$CdCu_3Ti_4O_{12}$	409	0,093
$La_{2/3}Cu_3Ti_4O_{12}$	418	0,060
$Sm_{2/3}Cu_3Ti_4O_{12}$	1665	0,048
$Dy_{2/3}Cu_3Ti_4O_{12}$	1633	0,040
$Y_{2/3}Cu_3Ti_4O_{12}$	1743	0,049
$Bi_{2/3}Cu_3Ti_4O_{12}$	1871	0,065
$BiCu_3Ti_3FeO_{12}$	692	0,082
$LaCu_3Ti_3FeO_{12}$	44	0,339
$NdCu_3Ti_3FeO_{12}$	53	0,325
$YCu_3Ti_3FeO_{12}$	33	0,308

All these compounds crystallize in the perovskite-related structure and adopt the Im3 space group symmetry, which is not common since tilting generally leads to the unit cell assymmetry.[17]

1.4. $CaCu_3Ti_4O_{12}$

Calcium copper titanate, commonly known as CCTO, has been extensively studied due its unusual electrical properties. It was firstly reported by *Subramanian et al.*[17] as a material with high dielectric constant of about 12000 at 1 kHz over a large temperature range 100 - 600 K. Nevertheless, CCTO displays a significant drop in the dielectric permittivity by a factor of 100, at a temperature below 100 K and frequency above 10^5 Hz.[18] These properties make CCTO a promising material in the capacitors industry. CCTO exhibits a cubic structure and belongs to space group Im3. Unlike most perovskite compounds displaying octahedral tilting, CCTO remains centrosymmetric. The octahedral tilt is designed by $a^+a^+a^+$ in Glazer notation and occurs to produce a square planar environment around Cu^{2+}. The distortion occurs by tilting of all Ti-O-Ti angles, which are significantly reduced to 141°, compared with 156° observed in orthorhombic $CaTiO_3$.[17,18] The tilting is accompanied by cation ordering and therefore the unit cell is doubled, as shown in figure 1.3, where the Ca^{2+} and Cu^{2+} cations are illustrated by blue, Ti^{4+} cation by grey and O^{2-} anion by red. The tilted TiO_6 octahedra is represented in green color.[19]

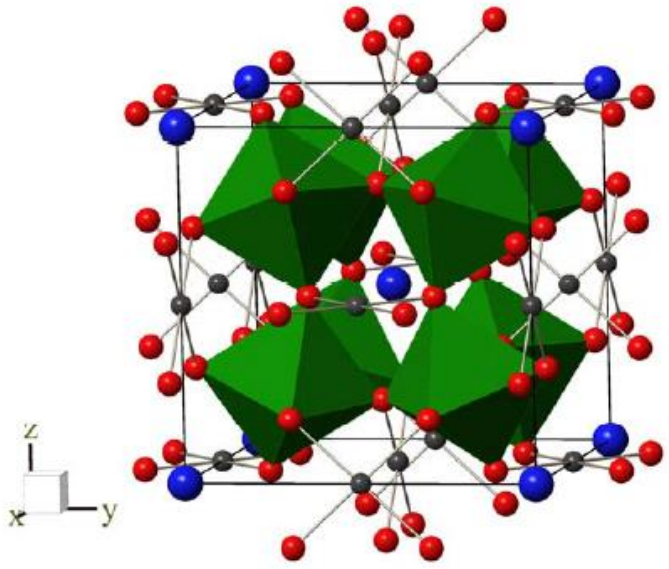

Figure 1.3 – Representation of the CCTO unit cell.[19]

1.5. Physical properties of CCTO

As mentioned before, CCTO has a very high dielectric constant which is fundamental to the production of smaller capacitors. Like CCTO, there is a wide range of perovskite compounds with high value of dielectric permittivity. But, interestingly, unlike other perovskite compounds, the dielectric constant of CCTO shows a different trend. CCTO exhibits a dielectric constant almost unchangeable over a large temperature range 100 - 600 K at radio frequencies. Below 100 K, however, this property drops significantly by a factor of 100, without any phase transition.

In other compounds, the dielectric constant depends on the temperature and usually assumes lower values when compared to CCTO. Figure 1.4 shows the dielectric permittivity of CCTO and BT ($BaTiO_3$) as a function of temperature at 1 MHz, where it is possible to observe the trend of dielectric constant as described in references.[4,20]

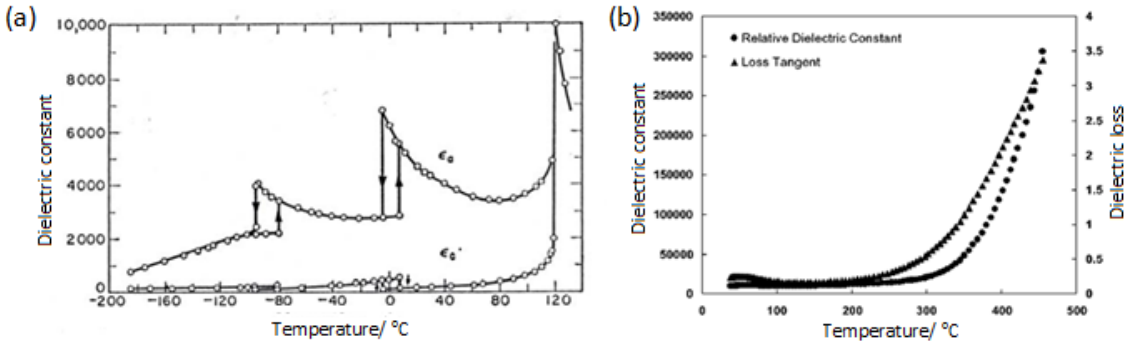

Figure 1.4 – Variation of the dielectric permittivity of (a) BT and (b) CCTO with temperature, at 1 MHz.

The different trend might suggests therefore that the mechanism responsible for the high dielectric permittivity in CCTO is different from the other compounds. In fact, this property is usually associated to an intrinsic or bulk effect giving two different classes of materials: ferroelectrics and relaxor ferroelectrics.

A ferroelectric material exhibits a dipole moment in the absence of an external electrical field. It is the case of $BaTiO_3$, in which the Ti^{4+} cation is displaced from the center of its octahedron, leading to the formation of a permanent dipoles responsible for the high dielectric permittivity values.[3,4]

A relaxor ferroelectric material exhibits a ferroelectric response under higher electric fields at low temperatures, but, without macroscopic spontaneous polarization.[6] Unlike ferroelectrics, the peak position of a relaxor ferroelectric material is a function of frequency and not accompanied by a structural transition.[17]

CCTO does not exhibit any of these mechanisms. Hence, structural considerations must be taken into account to understand why CCTO displays such a high dielectric constant. In the next section the $BaTiO_3$ structure, a classic ferroelectric material and widely used in the capacitor industry, is compared with CCTO.

1.6. Ferroelectric $BaTiO_3$

$BaTiO_3$ (BT) has been used for more than 60 years due to its ferroelectric properties combined with chemical and mechanical stability and ease of mass production.[21] For this report, only the ferroelectric properties of BT responsible for the high dielectric constant are discussed and compared with CCTO.

BT belongs to the family of perovskites and shows displacement of the Ti^{4+} cation within the TiO_6 octahedra, as shown in figure 1.5, where Ti^{4+} is represented by the green sphere.[13]

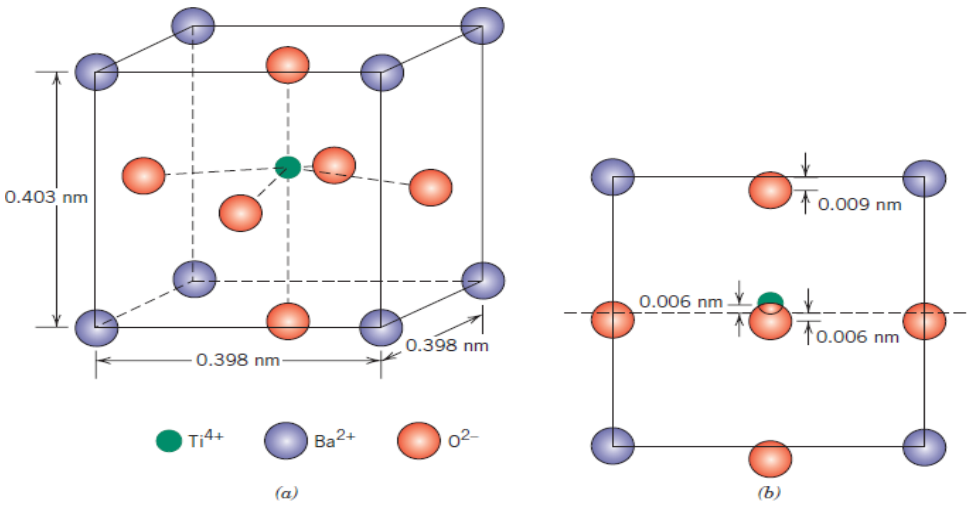

Figure 1.5 – BT unit cell displaying Ti^{4+} displacement.[22]

BT displays spontaneous polarization because the Ti^{4+} is displaced off its central position, and it has proved to be very successful in explaining its ferroelectric properties below the Curie temperature (T_c ~ 120 ^oC). Above T_c the unit cell undergoes a phase transition to become cubic and the high temperature non-polar phase is referred to as the paraelectric state, accompanied by an abrupt decrease in the dielectric constant.[21]

The high dielectric constant of BT is associated with three structural phase transitions on heating/cooling, each one corresponding to a peak, as shown in figure 1.4, section 1.5. The first transition occurs from rhombohedral to orthorhombic at - 90 ^oC; the second occurs at - 5 ^oC and transforms to tetragonal; finally and most important, at 120 ^oC (T_c), where the structure becomes cubic. Above T_c, BT transforms to a paraelectric state, where the structure consists of a cubic cell where all atoms occupy symmetric positions and, therefore, the ferroelectric state no longer exists leading to a significant drop in the dielectric constant.[17,21]

The displacement of the Ti^{4+} cation occurs because Ba^{2+} is larger than Sr^{2+} ($SrTiO_3$ is an ideal perovskite as referred in the section 1.2.2.1) resulting in an expansion of the structure, with increasing of Ti-O distance from 1,95 to 2 Å. The TiO_6 octahedra is now too large for Ti^{4+} and Ti-O bonds are under tension. On the other hand, the Ba-O distance of 2,99 Å based on the ionic radii is much higher than the experimental value of 2,84 Å, suggesting that Ba^{2+} is in a site small for it. This contributes to the increasing of polarizability of the TiO_6 octahedra and therefore to the Ti^{4+} displacement.[17]

1.6.1. Structural considerations of CCTO

CCTO, on the other hand, does not display polarizability since all atoms in the unit cell occupy symmetric positions. Therefore, CCTO is not a ferroelectric material. Like most perovskite compounds, CCTO exhibits octahedral tilting, however, it remains centrosymmetric.

Like BT, the Ca-O distance of 2,84 Å in CCTO based on the ionic radii is much higher than the experimental value of 2,60 Å. This also suggests that Ca^{2+} cation is in a site too small for it leading to the expansion of unit cell and Ti-O bonds are under tension. However, the site symmetry for Ti^{4+} in CCTO is much lower than that in cubic BT, reducing the possibility of any phase transition based on the displacement of Ti^{4+} within the octahedra. Instead, the TiO_6 octahedra have tilted to form a square arrangement around Cu^{2+}, in which the tilts are all in-phase, $a^+a^+a^+$, according to

Glazer notation. In fact, Ti-O-Ti angles show a significant reduction of 141^{o} compared to 156^{o} observed for $CaTiO_3$.[17,23]

1.7. High dielectric permittivity of CCTO

The mechanism responsible for the high permittivity of ferroelectrics, based on structural considerations, was discussed above. For CCTO no ferroelectric property has been found. So far, this reason has attracted several researchers to try to understand why CCTO displays such high dielectric permittivity.

Different models have been proposed to explain the origin of the high dielectric permittivity in CCTO. Some of them suggest intrinsic models; however, most studies support an Internal Barrier Layer Capacitance (IBLC) mechanism, an extrinsic model, as the main source responsible for the high dielectric permittivity. Some researchers, however, link the high dielectric permittivity to a non-ohmic electrode-semiconductor contact.

1.7.1. Non-ohmic contacts

A non-ohmic contact does not follow the Ohm's law, V = RI, due to a mismatch in the Fermi level at the interface between two materials with different composition, leading to the formation of a blocking or Schottky barrier at the interface. This prevents the mobile charge carriers in the junction of the two materials, giving rise to a high permittivity value. Figure 1.6 shows the energy band for a metal and an n-type semiconductor, in separated and in contact. Φ_m represents the work function of the metal and consists of the energy required to remove an electron with the Fermi energy to the 'vacuum level'. Φ_s represents the effective work function of the semiconductor and corresponds to the energy difference between the Fermi energy and the vacuum level. It is assumed for an n-type semiconductor that $\Phi_m > \Phi_s$. When the metal and semiconductor are in contact, the electrons flow from the semiconductor to the metal until the Fermi energy becomes constant. The electrons moving from the semiconductor to the interface find an energy barrier (the Schottky barrier) of height $|e|U_b$, which determines the electrons crossing the barrier and it is given by:

$\Phi_b = \Phi_m - \Phi_s$ (3)

At equilibrium, the thermally excited electron current from a metal to a semiconductor and from a semiconductor to a metal are equal.[24,25]

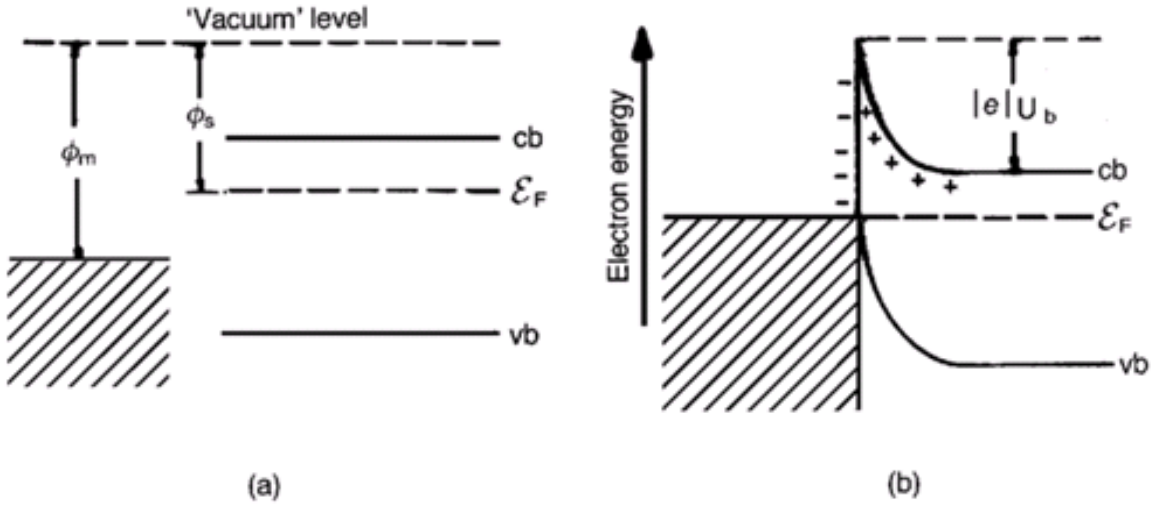

Figure 1.6 – Energy band diagrams for a metal and an n-type semiconductor: (a) the two materials are separated and (b) the materials are in contact.[26]

Most researchers do not agree with the non-ohmic contact as the main source responsible for the high dielectric permittivity since it seems not to be dependent on the electrode material. However, *Lunkenheimer et al.*[26] studied the effect of the electrode metal by using brass plates, silver paint and sputtered gold and silver. Results showed that the dielectric permittivity is dependent on the electrode applied. The effect of thickness was also studied on samples with 0,69 and 0,24 mm of thickness, and the dielectric permittivity also showed a dependence on that. This study also explains why CCTO displays so many values for dielectric permittivity in the literature: contacts formation between the electrode and the sample as surface roughness and type of contact may have a substantial effect on the permittivity.

1.7.2. Internal barrier layer capacitance (IBLC)

Considered the most plausible model to explain the high permittivity of CCTO, the IBLC model consists of the presence of a resistive thin grain boundary. Unlike most IBLC materials, CCTO needs only a single step processing at relative low temperatures in air to produce the resistive thin layer.[27] This phenomenon has surprised researchers since this effect is usually obtained by a multi-stage processing based on limited reoxidation of a reduced composition at high temperatures, resulting in a surface layer of high resistivity surrounding a conducting core and giving rise to a large effective permittivity. For example, the ferroelectric $BaTiO_3$ used in the production of IBLCs with ε_{eff} values between ~ 20 000 and 50 000 is obtained by this complex process.[27] The simplified structure of an internal barrier layer capacitor ceramic is shown in figure 1.7.

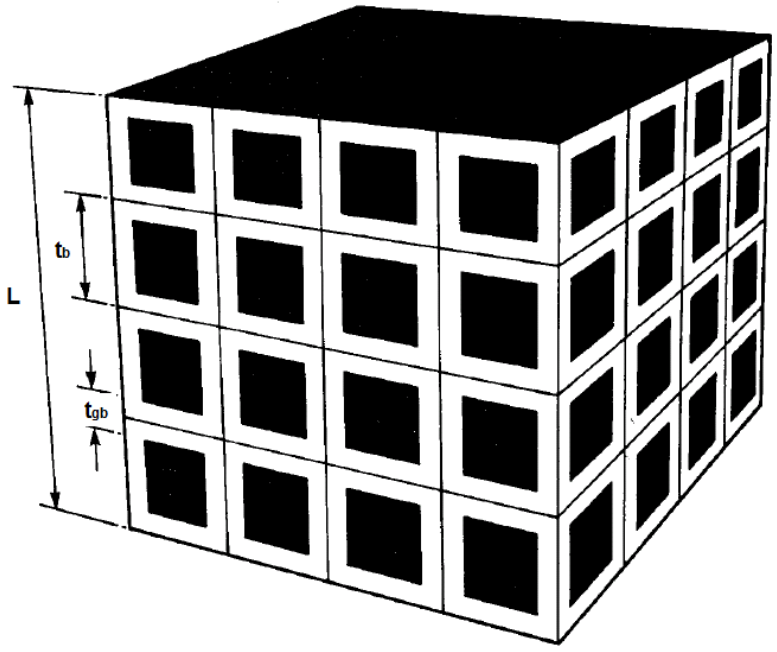

Figure 1.7 – Representation of the simplified IBLC: t_b is the bulk thickness, t_{gb} the grain boundary thickness and L the sample thickness.

In the IBLC model, the term effective dielectric permittivity, ε_{eff}, is used instead of dielectric permittivity, normally related to an intrinsic property. The ε_{eff} of an IBLC can be estimated as follow:[28]

$$\varepsilon_{eff} \approx \varepsilon_r \frac{t_b}{t_{gb}} \quad (4)$$

where ε_r is the intrinsic permittivity of the material, t_b and t_{gb} are the thickness of the bulk and grain boundary regions, respectively.

This model was supported by several studies where different techniques were applied in order to understand the mechanism responsible for the high ε_{eff}. *Sinclair et al.* [29] studied the electrical properties of CCTO using impedance spectroscopy, where data showed CCTO ceramics to be electrically heterogeneous, consisting of semiconducting grains surrounded by insulating grain boundaries. Grain and grain boundary resistivities at 300 K were 60 Ω cm and 450 kΩ cm, respectively, consistent with an IBLC model. In terms of data, impedance complex plane plots, Z*, at 300 K consist of a large arc at low frequencies with a non-zero intercept on the Z' axis at high frequency.

Kim et al.[30] studied the dc bias dependence of the grain boundary resistance for different voltages at 210 ^{o}C. The data showed that the interception of the large arc at high frequencies does not vary with applied dc bias, consistent with the ohmic resistance in grains. The arc corresponding to the grain boundary response, on the other hand, was shown to be dc bias dependent. The resistivity decreases with increasing dc bias, indicating that Schottky barriers might be present at the grain boundaries.

Chung et al.[31] examined the presence of a potential barrier at the grain boundaries by using microcontact current-voltage measurements. The I-V characteristics were directly measured across individual grain boundaries and within the grains. Again, the grains obeyed Ohm's law, whereas, the I-V measured across grain boundaries was nonlinear, consistent with the presence of an electrostatic barrier at the grain boundaries. In this work, the authors also determined the breakdown of CCTO as a function of the grain size for samples sintered at 1100 ^{o}C for 3 and 20 h. The breakdown voltage decreased significantly from 1300 to 300 V cm^{-1}, respectively. This dependence is related to internal interfaces acting as electrical potential barriers and might be the grain boundary.

Although the IBLC model is now widely accepted as the main source responsible for the high effective permittivity in CCTO ceramics, questions relating to the development of the n-type semiconductivity of CCTO are still unclear, since the formula $CaCu_3Ti_4O_{12}$ corresponds to a stoichiometric composition and, therefore, the grains should be insulating. Two models have been proposed to explain the origin for bulk semiconductivity in CCTO ceramics.[32] Both are, naturally,

based on non-stoichiometry of the bulk composition, occurring at the high temperatures required for CCTO processing. Probably, the semiconducting grains appear during calcination in the temperature range of 950 - 1100 ^{o}C and/or during the sintering process that requires high temperature to get dense CCTO ceramics. The first model involves oxygen loss and the second is based on cation non-stoichiometry. The difficulty in identifying the mechanism responsible for the grain semiconductivity arises from the very small deviation of stoichiometry which is difficult to detect by conventional techniques. For example, a CCTO sample was subjected to thermogravimetric (TG) analysis up to 1100 ^{o}C showing no significant weight loss on heating and cooling, confirming therefore that a small amount is lost, however, enough to induce bulk semiconductivity in CCTO ceramics.[29]

1.7.2.1. Oxygen non-stoichiometry model

Oxygen loss is a plausible model to explain the origin of the bulk semiconductivity in CCTO ceramics, based on a comparison with other titanate-based perovskites in which this phenomenon is present when samples are processed at high temperatures and under inert/reducing atmospheres. Basically, a small amount of oxygen is lost from the unit cell of CCTO during processing in air at moderate temperatures, typically in the range of 900 - 1100 ^{o}C, with subsequent compensation of oxygen vacancies by introduction of electrons into the Ti 3d band. The oxygen lost to the atmosphere is represented by the following equation:

$$O_O^x \rightarrow \frac{1}{2}O_2 + V_O^{\cdot\cdot} + 2e' \qquad (5)$$

This process results in the general formula $CaCu_3(Ti_{4-x}^{4+}Ti_x^{3+})O_{12-\frac{x}{2}}$.[32]

1.7.2.2. Cation non-stoichiometry model

Cation non-stoichiometry comprises two steps, occurring separately. The first step on heating and the second on cooling. During heating, a reduction of Cu^{2+} to Cu^{+} with subsequent charge compensation by partial occupation of excess Ti^{4+} on the Cu sites occurs. The second step, on

cooling, consists of limited reoxidation of the monovalent copper to Cu^{2+} where the charge compensation is ensured with electrons entering the Ti 3d conduction band and, therefore, a partial reduction of Ti^{4+} to Ti^{3+} occurs. The following reactions describe, respectively, the first and second steps:

$$3Cu^{2+} \rightarrow 2Cu^{+} + Ti^{4+} \quad (6)$$

$$Cu^{+} + Ti^{4+} \rightarrow Cu^{2+} + Ti^{3+} \quad (7)$$

The first reaction gives rise to the general formula $Ca(Cu^{2+}_{1-3x}Cu^{+}_{2x}Ti^{4+}_{x})_3Ti_4O_{12}$ and, the second, to $Ca(Cu^{2+}_{1-x}Ti^{4+}_{x})_3(Ti^{4+}_{4-6x}Ti^{3+}_{6x})O_{12}$.[32]

1.8. Influence of microstructure on the electrical properties of CCTO ceramics

As mentioned before, the high effective permittivity of CCTO ceramics is related to an IBLC where a thin resistive layer at the grain boundaries seems to be responsible for this property. The ε_{eff} has been shown, however, to be dependent on the microstructure, which in turn depends on the processing conditions of synthesis and sintering such as time, temperature, cooling rate and oxygen partial pressure. This is why a wide range of values for ε_{eff} (4 000 – 300 000) is reported in the literature for CCTO ceramics.

It is well known from the fundaments of sintering that longer time and temperature of sintering usually results in larger grains. *Sinclair et al.*[27] studied the effect of the grain size on the ε_{eff}, where two samples were sintered at 1100 °C in air for 3 and 24 h. The average grain size was, respectively, 5 and 100 µm, resulting in the enhancement of ε_{eff} from ~ 9 000 to 280 000. Smaller average grain sizes have a larger volume fraction of grain boundaries and therefore Schottky barriers, resulting in an increase of the effective thickness of the charge storage regions, which produces smaller values of ε_{eff}. Nevertheless, the grain boundary resistivity decreased from 4,2 to 0,18 MΩ cm. The bulk resistivity decreases from ~ 70 to 30 Ω cm due to the decomposition of CCTO as discussed in the section before. On the other hand, larger grains originate higher dielectric losses.

In another study provided by *Sinclair et al*.[28], sintered pellets were heat treated in N_2 at 1000 ^{o}C. The Z* plots showed the grain resistivity not to be dependent on the treatment with a R_b ~ 60 Ω cm. The grain boundary resistivity, however, decreased two orders of magnitude from ~ 450 to 7 kΩ cm, revealing that R_{gb} is dependent on the oxygen partial pressure of processing. These results reveal that reoxidation of the grain boundary in air might occur on cooling, producing a resistive thin layer responsible for high ε_{eff} of CCTO ceramics.

He et al.[33] studied the effect of cooling rate on the electrical properties. The permittivity of the samples seems not to be dependent on the cooling rate. However, the grain boundary resistivity is reduced as the cooling rate increases, and the dielectric loss rises. Apparently, the cooling rate affects the reoxidation process causing changes in the electrical properties of CCTO ceramics.

Bender et al.[34] prepared CCTO by conventional solid state reaction, mixing the initial reagents by two different routes: via mortar and pestle and attrition-milling. It was observed that the high permittivity of CCTO ceramics prepared via mortar and pestle were 11 700, much lower compared to those prepared by attrition milling, 100 000. The effect of sintering temperature for ceramics prepared by attrition-milling was also studied for 990 and 1050 ^{o}C, giving rise to dielectric constants of 714 and 82 450, respectively.

Yang et al.[35] studied the electrode/sample contact effects on the dielectric properties of CCTO ceramics. They associated the high dielectric constant, in part, to the electrode/contact effects, depending on the surface resistivity of the samples. For samples whose surface resistivity is higher than 1,2 x 10^8 Ω cm, the dielectric properties are independent of the metal electrodes and sample thickness. A subsequent annealing of the samples in N_2 atmosphere at 750 ^{o}C led to a decrease of the surface resistivity down to 3,1 x 10^7 Ω cm, where the dielectric properties have become changeable according to the metal electrodes. The dielectric constant of the sample with Pt electrodes showed a higher value compared to that with Ag electrodes.

Kwon et al.[36] have investigated the effects of cation stoichiometry on the electrical properties of $CaCu_{3-x}Ti_{4-y}O_{12}$ (x= +0.06, 0, -0.06; y= +0.08, 0, -0.08) prepared by solid state reaction. X-ray diffraction revealed that both Cu- and Ti-excessive CCTO compositions showed the presence of a secondary Cu_2O phase in the interior of non-stoichiometric CCTO ceramics giving rise to lower dielectric constants compared with stoichiometric CCTO ceramics. The compositions corresponding to Cu- and Ti-deficient CCTO showed no secondary phases and higher dielectric constants and losses compared to the stoichiometric composition.

1.9. Doping effects in CCTO ceramics

Several doping studies of the initial composition of CCTO have been performed in order to improve the electrical properties and at the same time to improve the understanding of the electrical properties displayed by undoped CCTO ceramics. As mentioned before, CCTO is electrically heterogeneous composed by a semiconducting grain and insulating grain boundary, with permittivities of ~ 100 and 10^4 - 10^5, respectively. The typical activation energy of the bulk is approximately 0,07 eV and grain boundary is in the range between 0,54 and 0,76 eV.

Interestingly, some works report some dopants to stabilize the composition at high temperatures by keeping the bulk resistive with activation energy similar to the grain boundary of undoped CCTO.

These results led researchers to believe that CCTO ceramics consist of bulk and grain boundary regions with slightly different compositions. *Li et al.*[32], prepared CCTO ceramics by doping with 2% of Mn giving rise to the general formula $CaCu_{2.94}Mn_{0.06}Ti_4O_{12}$ (CCMTO). The electrical properties were investigated by impedance spectroscopy and fixed frequency capacitance measurements. The Z* plots for CCMTO at 473 K showed an absence of a nonzero intercept suggesting the bulk resistance to be significantly higher for CCMTO ceramics. In fact, Arrhenius plots of the σ_g and σ_{gb} for CCMTO showed that R_b is at least six orders of magnitude higher compared to that observed in undoped CCTO ceramics. The activation energy increases from ~ 0,08 eV for CCTO to ~ 0,63 eV for CCMTO, which is similar to that observed for the grain boundary in undoped CCTO ceramics. The bulk conduction mechanism in CCMTO is, therefore, similar to that observed for the grain boundary in CCTO. On the other hand, fixed frequency capacitance data showed that the 'giant permittivity' observed in CCTO is not observed for CCMTO, suggesting once more the bulk resistance to be much higher in CCMTO. These results may suggest that the origin for the semiconductivity of grains in CCTO ceramics is based on a slightly different composition between the grains and grain boundaries, however, enough to induce semiconductivity in the grains. In addition, cation-nonstoichiometry may be a plausible explanation for the origin of the semiconductivity. Partial substitution of Mn^{4+} instead of Ti^{4+} on the Cu sites may occur at high temperatures in CCMTO: on cooling, reduction of Mn^{4+} to Mn^{3+} may occur to compensate for the reoxidation of Cu^{+} in preference to partial reduction of the B-site Ti^{4+} to Ti^{3+} ions. This avoids the introduction of electrons to the Ti 3d conduction band and therefore decreases substantially the bulk semiconductivity.

Feng et al.[37] studied the effects of La doping on the A'-site, $Ca_{1-x}La_xCu_3Ti_4O_{12}$ (x = 0, 0.1, 0.2, 0.3, 0.4). They observed a decrease of the dielectric loss and dielectric constant as the La content increases. Impedance spectroscopic data showed the bulk conductivity to increase with La doping, while the grain boundary resistance remained nearly unchanged. The decrease in the dielectric loss was explained by the decrease in the resistivity of CCTO grains/subgrains as La^{3+} acts as a donor when it substitutes Ca^{2+}, increasing the electron concentration and therefore a decrease of the bulk resistance. In comparison, different results were obtained by *Varma et al.*[38] In their study of $Ca_{1-x}La_{(2/3)x}Cu_3Ti_4O_{12}$ (x = 0, 0.5,1), they concluded that La^{3+} substituting Ca^{2+} site resulted in the decrease of the bulk and increase of the grain boundary conductivities with increasing of La^{3+} content. Consequently, a decrease of the internal barrier layer effect was observed.

Doping CCTO has therefore revealed that the electrical properties of CCTO ceramics can be changed and controlled according to the properties desired. In addition, some works have shown that it is possible to keep the bulk resistive with the activation energy similar to the grain boundary of undoped CCTO ceramics and therefore, the conduction mechanism is similar. This led researchers to believe that bulk and grain boundary may consist of similar but slightly different compositions. At the same time, conventional techniques do not allow detection of variations in the bulk composition as they are very small and, hence, it is difficult to understand the mechanism responsible for the origin of the semiconducting grains. Therefore, no consensus is seen in the literature reporting which mechanism is responsible for this phenomenon. Moreover, these results lead researchers to believe that CCTO ceramics become unstable at intermediate temperatures (900 - 1100 ^{o}C) and its process involving the synthesis and sintering methods may be responsible for the appearance of semiconducting grains as always seen in the literature.

1.10. Aim of this work

Pure CCTO ceramics have been reported in the literature to consist of a semiconducting bulk surrounded by a thin resistive layer at each grain boundary and hence, described as an internal layer barrier capacitor (IBLC). CCTO, unlike most of compounds exhibiting these electrical characteristics, needs only a single step of processing at relatively low temperatures in air. The IBLC observed in most compounds is usually obtained by a multi-stage processing based on

limited reoxidation after a reducing process at high temperatures. This gives rise to the formation of a resistive layer surrounding a conducting core responsible for the large effective permittivity.
The electrical properties of CCTO, however, are still unclear since the start composition of CCTO is stoichiometric and therefore, the bulk should be resistive and not semiconducting. The literature has always reported CCTO to be described by an IBLC model. Therefore, questions relating to the processing of CCTO may be regarded in order to understand how it influences the electrical properties of CCTO ceramics.
The processing of CCTO ceramics can be essentially comprised by the synthesis and sintering processes. The most common method to synthesize CCTO powder is by solid state reaction. However, the temperature required to get pure CCTO is in the range between 950 and 1100 ^{o}C and it is possible that at these temperatures the grains become semiconducting. Therefore, other methods have been applied to produce CCTO powder at lower temperatures 800 - 900 ^{o}C. However, the sintering temperature required to get dense ceramics is very high at ~ 1000 - 1100 ^{o}C leading to the appearance of semiconducting grains.

The aim of this work is to produce CCTO powders by a non-conventional synthesis process at low temperatures, high-energy ball milling, and to characterize its impact on the electrical properties of CCTO ceramics. High-energy ball milling (HEBM) is a useful technique for synthesis of pure nano-materials. This method is a simple method for oxides synthesis and it has been used to produce homogenous and crystalline nanopowders. It is similar to the conventional solid state reaction, consisting in a first step of milling of the precursors with subsequent calcination. The difference is on the impact energy during milling. HEBM provides much higher impact energy due to the higher velocity of milling and may be eventually up to 1000 times higher compared to that achieved in conventional solid state reaction. This contributes for a reduction of crystallite size, efficient mixing of precursors and mechanical activation by structural changes.[39] This results in a decrease of the calcination temperature to produce a single-phase compound.

The objective of this work is to produce CCTO powders at low temperatures by high-energy ball milling and to understand if it is possible to produce pure CCTO ceramics with resistive bulk and, therefore, how it influences the electrical properties of CCTO ceramics. The electrical characterisation is provided using impedance spectroscopy (IS).

2. Experimental procedure

2.1. Preparation and structural characterisation of CCTO powders

Single phase CCTO was prepared by high-energy mechanochemical treatment of precursors: CuO (Merck, 99.0 %), $CaCO_3$ (Lancaster, 99.0 %) and TiO_2 (Aldrich, 99.8 %) in stoichiometric quantities. The reagents were weighed and mixed in a ball mill using yttria-stabilized zirconia grinding media at 650 rpm for up to 10 hours. Excess heating was avoided by milling for periods of 10 minutes with a pause for 3 minutes. The direction of rotation was reversed after each interruption. The progress of structural changes or onset of reaction products was monitored by XRD analysis of small fractions of the powders collected after different milling times.

The resulting powders obtained by mechanochemical treatment were calcined in air at 650 and 700 ^{o}C for 12 hours with a heating rate of 5 ^{o}C/min, to attempt complete conversion of precursor reactants according to the chemical reaction:

$$CaCO_{3\,(s)} + 3\,CuO_{\,(s)} + 4\,TiO_{2\,(s)} \longrightarrow CaCu_3Ti_4O_{12\,(s)} + CO_{2\,(g)} \quad (8)$$

The calcined powders were characterized by X-ray diffraction to monitor the presence of a single-phase CCTO and to obtain the lattice parameters and theoretical density from the data.

2.2. Phase analysis of calcined powder

The phase purity of calcined powder was studied by X-ray diffraction on a Rigaku Geigerflex diffractometer using Cu Kα1 radiation of wavelength 1,54059 Å. The powder was scanned in the 2θ range 20 – 60 ^{o}.

From XRD data, the lattice parameter and the theoretical density were determined. The d-spacing can be determined using Bragg's law as follow:

$n\lambda = 2d \sin\theta$ (9)

where n is the layers index number and usually takes value of 1, λ is the wavelength, d is the spacing between planes in the atomic lattice and θ is the angle between the incident ray and scattering planes.

CCTO belongs to the space group Im3 and, therefore, has a cubic unit cell structure. The relation between the lattice parameter, a, and the d-spacing is:

$$a = d\sqrt{l^2 + k^2 + h^2} \quad (10)$$

The volume of the unit cell is:

$V_{cell}=a^3$ (11)

And, finally, the theoretical density is:

$$d_{theoretical} = \frac{\sum M_A/N_A}{V} \ (g/cm^3) \quad (12)$$

where M_A is the atomic mass and N_A the atomic number.

2.3. CCTO ceramic processing

Green bodies of CCTO were pressed uniaxially in a steel die under an applied pressure of 200 MPa and then, sintered on a platinum foil in a furnace (Lenton) at different temperatures (700, 800, 900, 1000 and 1100 ^{o}C) in air for 4 hours. The heating and cooling rates were 5 ^{o}C min^{-1}. After sintering, the relative density of the pellets was measured from their geometry, according to the following equation:

$$\%d = \frac{\frac{M_{sample}}{V_{sample}}}{d_{theoretical}} \times 100 \quad (13)$$

2.4. Electrical characterisation

2.4.1. Impedance spectroscopy

To study the effect of synthesis and sintering conditions on the electrical properties of CCTO ceramics, impedance spectroscopy measurements were performed at high and subambient temperatures, i.e, at temperatures below room temperature.

Prior to measurements, CCTO samples were polished to make parallel surfaces to provide a better contact for the electrical measurements and the diameter and thickness of the pellets were measured using a micrometer to determine the geometric factor, L/A (cm^{-1}).

Subambient measurements were performed using an impedance analyzer (Agilent E4980) with an applied ac voltage of 100 mV, over a frequency range of 20 Hz - 2 MHz and a temperature range of 10 - 320 K in a closed-cycle He refrigerator. InGa (60:40) alloy was used as electrode on both faces of the pellet. IS data were corrected for sample geometry and analyzed using the commercial software package ZVIEW.

For high temperatures, Au electrodes were sputtered on each pellet face on an Emitech K575XD sputter coater. The measurements were taken in air using an Agilent 4294A impedance analyzer with an applied ac voltage of 100 mV over a frequency range from 10 Hz - 10 MHz and over a temperature range from 300 to 700 K. Data were corrected for sample geometry and analyzed using the commercial software package ZVIEW. The next sections provide the theory of impedance spectroscopy.

2.4.2. Fundaments of impedance spectroscopy [19,40,41,42,43]

Impedance spectroscopy (IS) is an important technique used to study correlations between electrical properties and microstructural features of materials. It is widely used, in part, because

the measurements are relatively quick but, mainly because it can be applied to different materials, without destroying the sample.

IS provides information not available from other traditional techniques such as dc and fixed frequency measurements, especially, in materials that are electrically heterogeneous. The electrical response obtained when a dc potential difference is applied, is the resistance to the overall system and, hence, does not permit to extract the values of individual regions of a material, for example, bulk and grain boundary resistances. Fixed frequency measures the electrical properties at a fixed frequency which does not allow analysis of different regions of a material since each one has its own frequency domain. A frequency range is, therefore, preferable so that different regions of a material can be characterised.

The heterogeneity of a material can be associated with a surface layer, inner and outer regions of individual grains and/or grain boundaries. Examples of electrically heterogeneous materials include solid electrolytes, dielectrics (e.g. piezo, pyro and ferroelectrics) and non-ohmic devices (e.g. varistors).

IS allows to optimize the materials processing by controlling the electrical properties. For example, in solid electrolytes characterised by ionic conductivity, it is important to get dense ceramics with low resistive grain boundaries in order to minimize the influence of current constrictions or blocking internal interfaces. On the other hand, materials such as internal layer barrier capacitors, ceramics are deliberately processed to get insulating grain boundaries whereas grain interiors are semiconducting and a high 'effective' dielectric constant can be achieved.

2.4.2.1. Theory

Impedance spectroscopy consists in the application of a known ac potential difference across a material, usually 100 mV, over a typical frequency range from 10^{-2} to 10^{7} Hz. The electrical response of the material must then be analyzed by an equivalent circuit, often consisting of a combination of resistors, R, and/or capacitors, C. The equivalent circuit is normally chosen according to some knowledge about the electrical microstructure of the material in question with some intuition that predicts the type of impedances expected. The equivalent circuit, however, consists in most of the cases, in series association of parallel RC elements. If more than one

electrical region in a material is present, for example, grain and grain boundaries are electrically different, they are usually connected in series, as shown in figure 2.1. The R_bC_b models the electrical response of the grain and $R_{gb}C_{gb}$ the grain boundary response. The overall sample resistance is the summation of R_b and R_{gb} which corresponds to the resistance obtained using dc electrical measurements.

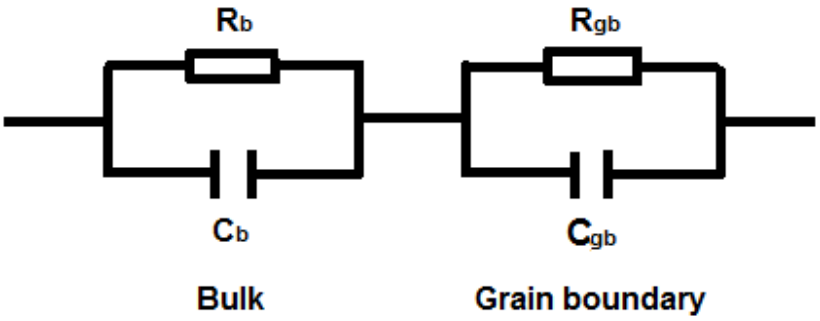

Figure 2.1 – Schematic of two parallel RC elements connected in series.

Some materials may show an additional electrical response due to the presence of other electro-active regions, for example, outer surface layers and electrode/sample contacts. This is usually described as a parallel RC element placed in series with those used to model the bulk and grain boundary regions.

Each element is composed by a resistive component, corresponding to the resistance, and a reactive component, corresponding to the capacitance and/or inductance. The inductance displays, however, a minimal effect in non-magnetic materials and can therefore be ignored. The reactance is therefore represented only by the capacitor.

Each region of a material is characterised by a relaxation time or time constant, τ, given by the following equation:

$$\tau = RC = 1/\omega_{max} \quad (14)$$

where $\omega_{max}=2\pi f_{max}$ is the angular frequency of the maximum loss. These parameters are important since they are independent of the geometry of a region within the material.

2.4.2.2. Impedance response of circuit elements

The impedance of a circuit element is defined by:

$$Z = \Delta V / \Delta I \quad (15)$$

For a pure resistor, the resistance follows the Ohm's law:

$$R = V/I \quad (16)$$

where V is the potential difference and I the current intensity. The response is not dependent on the potential difference, i.e, it is the same under an ac or a dc potential field.

On the other hand, capacitors and inductors are dependent on the applied frequency (ω) according to the equations, respectively:

$$X_C = 1/\omega C \quad (17)$$

$$X_L = \omega L \quad (18)$$

C is the capacitance and L the inductance.

2.4.2.3. Impedance formalisms

IS data can be represented by different formalisms, each one highlighting a different aspect of the data. There are four different possible formalisms: impedance Z*, admittance Y*, permitivity Ɛ*, and electric modulus M*. The most common plot is that one represented by impedance, Z*= Z - Z'' which has a real part, Z', and an imaginary part, Z''. The amplitude of Z' is related to the resistive part and the peak of Z'' to the capacitor. Figure 2.2 shows a general impedance plot.

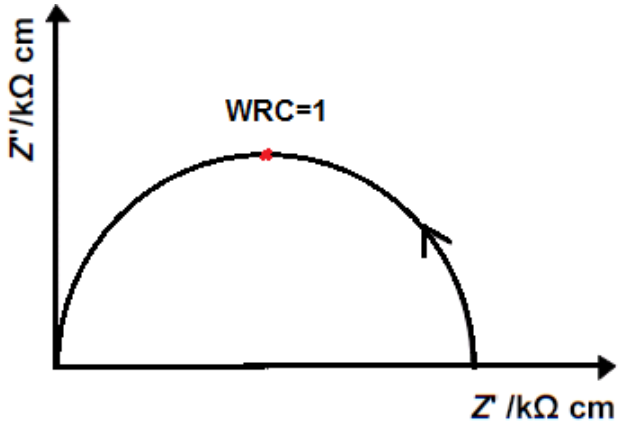

Figure 2.2 – Typical Z* impedance plot.

The others complex formalisms are represented by:

$$M^* = j\omega C_0 Z^* \quad (19)$$

$$\varepsilon^* = 1/M^* \quad (20)$$

$$Y^* = j\omega C_0 \varepsilon^* = 1/Z^* \quad (21)$$

where $C_0(L/A)=\varepsilon_0=8.854\text{x}10^{-12}$ F m^{-1} is the permittivity of vacuum.

2.4.2.4. Combined ideal circuit elements

Different regions of a material are characterised by different values of resistance and capacitance, usually placed in parallel. When the corresponding relaxation frequencies $1/(R_iC_i)$ differ by orders of magnitude, each parallel RC element gives rise to a semicircle from which the values of R and C can be extracted. The value of R is obtained from the interception of the semicircle on the Z' axis and, C, using the equation (14) at the maximum of each semicircle.

The determination of the capacitance values is very important, since each region in a material has its own typical values and, therefore, it is possible to assign the capacitance to the respective region. Table 2 shows typical capacitance values for different phenomena within a material.

Table 2 - Possible phenomena and their typical capacitance values.[19]

Phenomenon responsible	Capacitance/ F cm^{-1}
Bulk	10^{-12}
Minor, second phase	10^{-11}
Grain boundary	10^{-11} - 10^{-8}
Bulk ferroelectric near T_c (Curie Temperature)	10^{-10} - 10^{-9}
Surface layer	10^{-9} - 10^{-7}
Sample-electrode interface	10^{-7} - 10^{-5}
Electrochemical reactions	10^{-4}

2.4.2.5. Single parallel RC element

A single parallel RC element is related to the bulk response, where R_b is the bulk resistance and C_b bulk capacitance. The response in the Z* plane for a single parallel RC element ideally takes the form of a semicircular arc which intercepts the origin at high frequency and the real axis at low frequency. Figure 2.3 shows a typical Z* plot for a single parallel RC element.

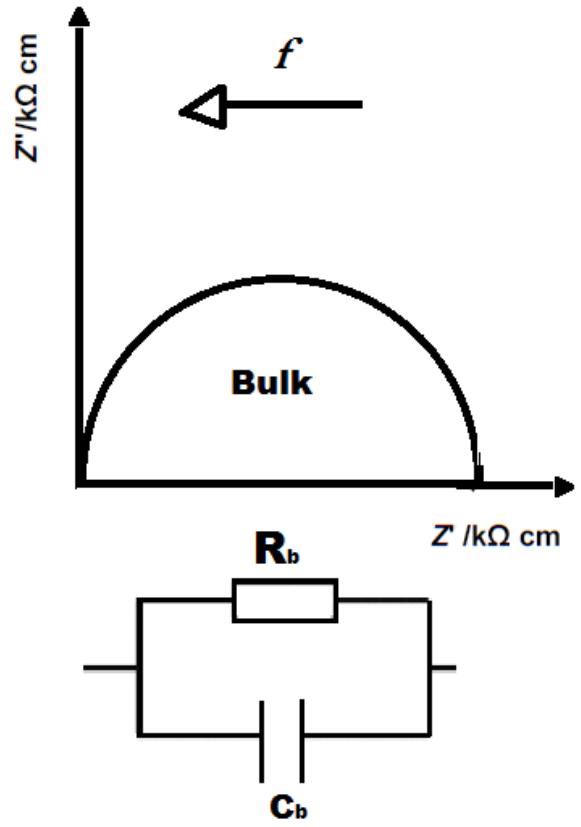

Figure 2.3 – Typical Z* plot and equivalent circuit for a single parallel RC element.

The semicircle associated with the bulk response in the Z* plots is usually depressed and therefore deviates from the ideal behaviour. This may be associated with the presence of a distribution in relaxation times within the bulk response and distortion by other relaxations, e.g., grain boundary relaxations, whose time constants are within two orders of magnitude of that of the bulk.

From the Z* plot it is possible to extract the value of R which corresponds to the diameter of the semicircle, also equal to the low frequency intercept on the Z'-axis or double the height of Z''_{max}. A geometry correction, L/A (cm^{-1}), is applied so that R and C values for different samples from the same or different materials can be compared.

An alternative presentation of the data is combining Z'' and M'' with the frequency, which can provide additional information not easy to extract from Z* plots, namely for materials with semiconducing grain interiors and very resistive grain boundaries. These plots are useful in assessing the electrical homogeneity of the bulk and determine as well the R_b and C_b values. Figure 2.4 shows a typical combined Z'' and M'' plot for a single parallel RC element. R_b is equal to twice the Z'' peak maximum, Z''_{max}, whereas C_b is the inverse of twice the M'' peak maximum, M''_{max}. The homogeneity is probed if both peaks appear at the same frequency.

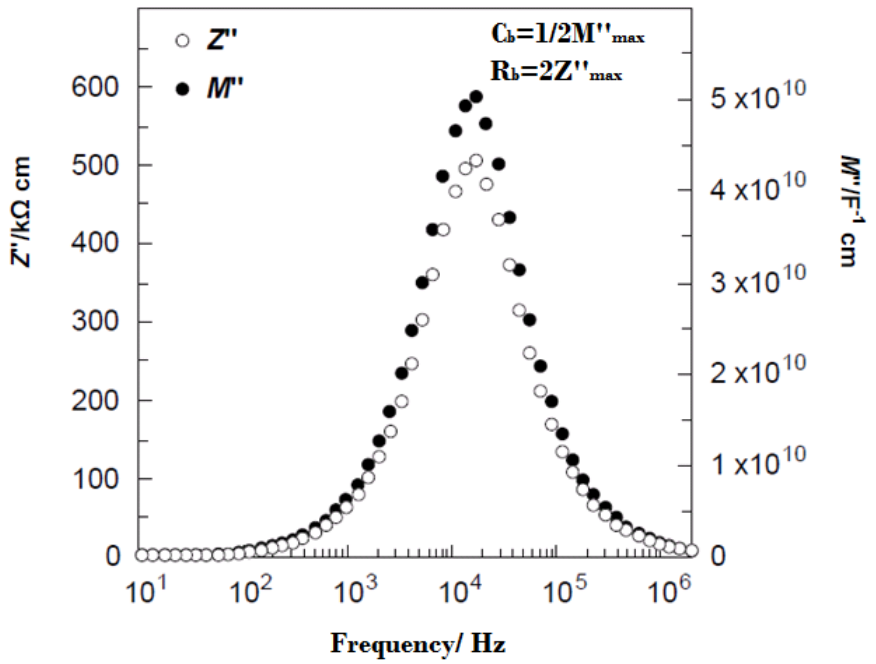

Figure 2.4 – Typical combined Z'' and M'' spectroscopic plot for a single RC element.[19]

2.4.2.6. Two parallel RC elements in series

Two parallel RC elements are studied in electrically heterogeneous materials with two distinct regions, usually associated with the grain and grain boundaries. Both are modeled by a parallel RC element and connected in series.

For example, in dense polycrystalline ceramics, grain boundaries can significantly influence the electrical properties of the material and it is observed in many electronic and ionic conducting ceramics. The Z* plot is similar to that observed for a single parallel RC element but ideally with two semicircles. The separation of the two semicircles depends on the difference of the time constant of each region. Ideally they should vary by 3 orders of magnitude to obtain a clear separation. Figure 2.5 shows a general Z* plot for a circuit consisting of two parallel RC elements in series.

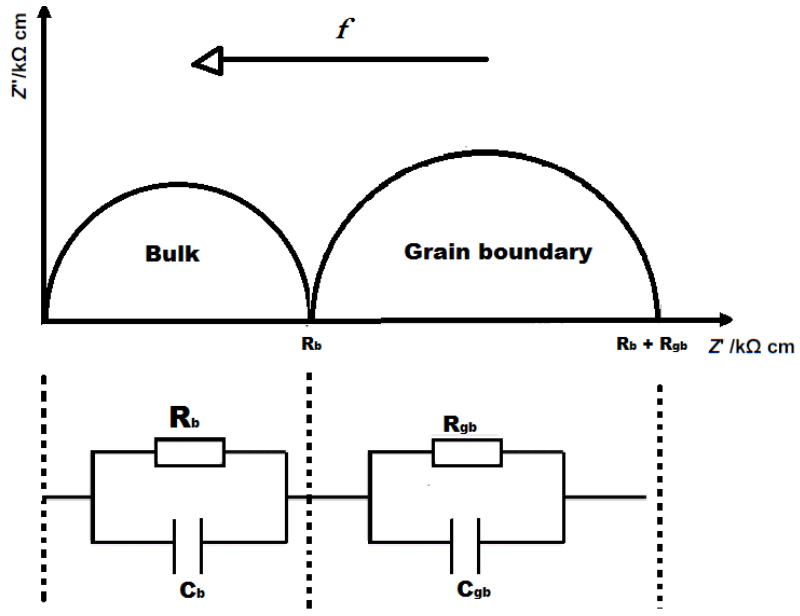

Figure 2.5 - Typical Z* plot and equivalent circuit for two parallel RC elements connected in series.

The Z* plot consists in two semicircular arcs. The arc at low frequency corresponds to the grain boundary response and the arc at high frequency to the bulk response. To determine the R and C

values for each region, the two semicircular arcs are treated separately, with the same method used for a single parallel element. The only difference is for determining the R_{gb}, since the lowest frequency intercept on the Z' axis is equal to the summation of R_b and R_{gb}.

In some cases, it may happens that one of the regions dominates the overall impedance spectra or that the time constant of each region does not permit their separation in Z* plots. In these situations, it is not easy to extract information about the electrical response of the grain and grain boundary individually from Z* plots. Therefore, a combined Z'' and M'' spectroscopic plot is useful to get information of both contributions. Figure 2.6 shows a general plot for two parallel RC elements connected in series.

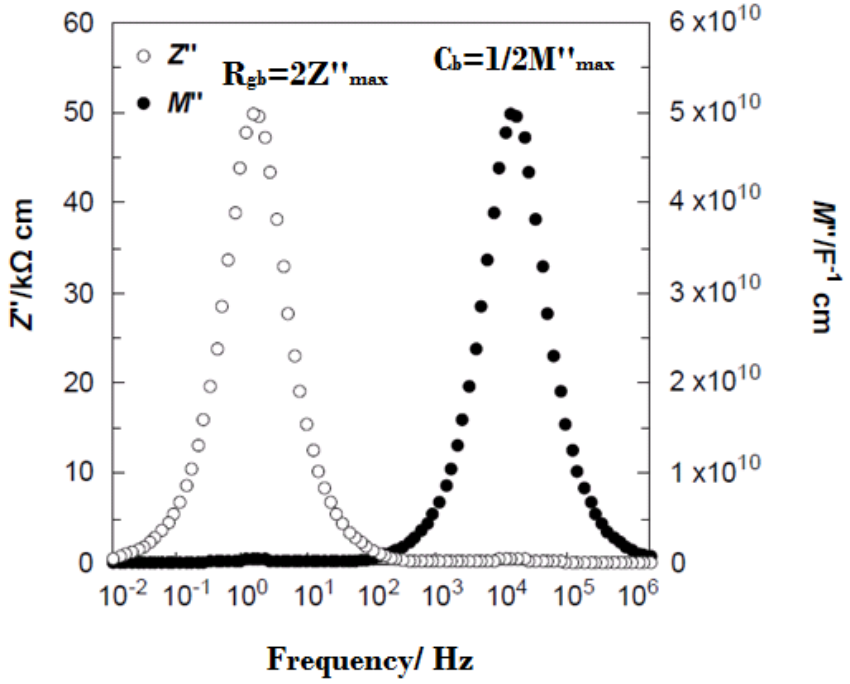

Figure 2.6 –Typical Z'' and M'' spectroscopic plot for two parallel RC elements connected in series.[19]

For each parallel RC element, a Debye peak occurs in both Z'' and M'' plots, permitting to identify the bulk and grain boundary regions of a material since Z''_{max} is half of the resistance and therefore dominated by the most resistive region; and M''_{max} is inversely proportional to the double of capacitance and hence, dominated by the lowest capacitive element, usually the bulk.

2.4.2.7. The Brickwork Layer Model [44 ,45]

The Brickwork Layer Model (BLM) is a model developed to interpret the IS spectra in materials where the grain boundary is electrically resistive and the bulk semiconducting. BLM assumes grains having cubic shape and perfect contacts between them, surrounded by identical thin resistive grain boundary layers in all of the ceramic. Although the BLM is considered an appropriate model to describe the electrical response of a material, some limitations are associated because these assumptions in practice are not respected. A very important consideration must be taken into account and is related to the values of resistance and capacitance of the regions within the material. When the electrical properties of samples are measured, the geometric factor, L/A (cm^{-1}) where L is the thickness and A the lateral area of the electrode, is applied to account for the effects of sample geometry and to obtain the relevant material properties (i.e. resistivity and permittivity). However, the geometric factor is a macroscopic value and, therefore, the specific resistivity and permittivity of the grain boundary vary significantly from the values determined, giving rise to much higher apparent permittivity $C_{gb}(L/A)$ and lower resistivity $R_{gb}(A/L)$ than they actual are. The capacitance and resistivity for bulk can be considered a good approximation since the grains comprise the majority of the sample, except possibly for nanomaterials.

2.4.2.8. Arrhenius plots

Arrhenius plots are useful to determine the activation energy of conduction, E_a, of a material. The comparison of E_a within the same material allows to identificate if the conduction mechanism is the same, for example, when samples of the same material are subjected to different processing. It may also assists the interpretation of different microstructural contributions ascribed to internal or external interfaces, etc. The conductivity of a material is thermally activated where it usually obeys the Arrhenius equation:

$$\sigma = \sigma_0 e^{(-\frac{E_a}{KT})} \quad (21)$$

where σ is the conductivity, σ_0 is a pre-exponential factor, k is the Boltzmann constant ($1{,}38 \times 10^{-23}$ J K^{-1}) and T is the absolute temperature. E_a is found from the linear slope when log(σ) is plotted against 1000/T.

2.5. Microstructural characterisation

In order to analyse the chemical evolution of CCTO ceramics with sintering process, a pellet sintered at 1100 ^{o}C was analyzed by scanning electron microscopy (SEM) using a JEOL 6400 and a backscattered electron image (BEI) was performed to identify the presence of any secondary phases. The chemical composition was also analyzed by energy-dispersive X-ray spectroscopy (EDS).

The pellet was ground and then polished with diamond paste down to 1 μm. Carbon coating was used as conducting surface to avoid charging under the electron beam.

3. Results and discussion

In this chapter, the results of the experimental work are shown and a brief discussion as they are presented is performed. Subsequently, an extensive discussion is done. The chapter is divided into two sections: the first presents a composition and microstructure characterisation of the CCTO compound. The second section approaches the electrical properties characterisation by impedance spectroscopy of the samples to evaluate the effect of the high-energy ball milling and sintering temperature on the electrical properties of CCTO ceramics.

To simpifly the identification of samples, they are denominated as shown in the table below with the respective relative density.

Table 3 – Identification of the samples sintered at different temperatures and respective relative density.

Sintering temperature (^{o}C)	Denominated sample	Relative density (%)
700	CCTO 700	57
800	CCTO 800	61
900	CCTO 900	72
1000	CCTO 1000	90
1100	CCTO 1100	86

3.1. Results

3.1.1. Structural and microstructural characterisation of CCTO

Structural changes of precursor powders obtained after different times (1, 2, 4, 6 and 10 h) of mechanochemical treatment were characterised by XRD (fig 3.1), and a gradual amorphisation of reactants is observed. In figure 3.1. for 1, 2 and 4 h of milling, it is possible to observe the peaks associated to the presence of TiO_2 and CuO and their gradual amorphisation as the time of milling increases. The data does not show evidence of $CaCO_3$, probably because its relative amount is too small and, also, because carbonates are usually amorphous. After 6 h of milling, the data shows the presence of an intermediate phase of $CaCu_2O_3$. Onset of XRD reflections ascribed to CCTO are hardly seen, even after 10 h of milling. Nevertheless, mechanochemical treatment promotes conversion to single phase CCTO phase by calcination at relatively low temperatures, as shown in figure 3.1, for powders calcined at 700 ^{o}C, for 12 h. The powder calcined at 650 ^{o}C does not

promote the complete convertion to a single phase CCTO as the XRD data exhibits the presence of secondary phases of TiO_2 and CuO.

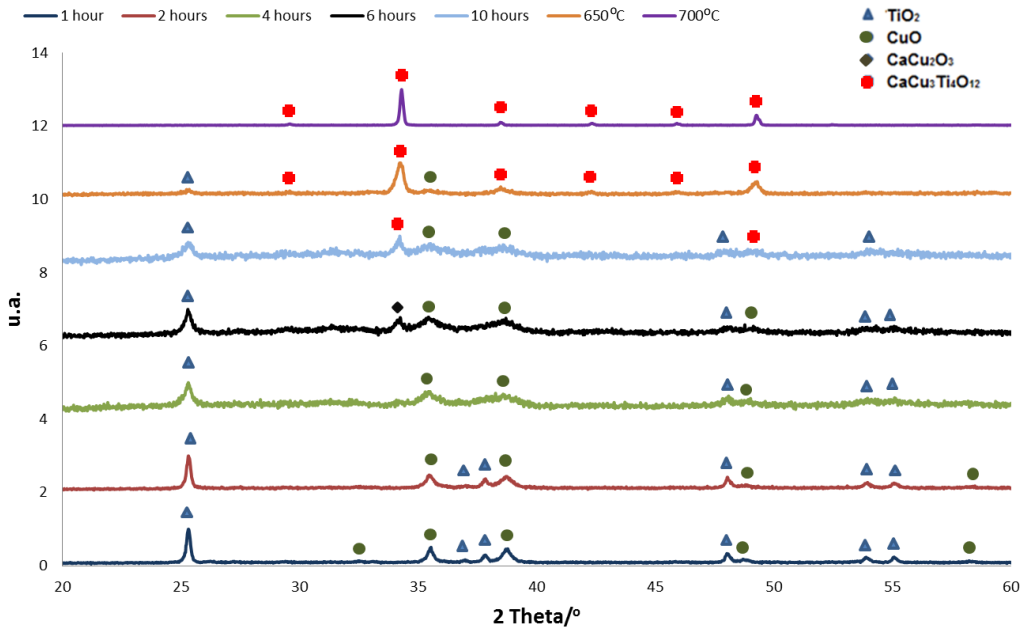

Figure 3.1 – XRD pattern of powders after milling for 1, 2, 4, 6 and 10 h, and after calcination at 650 and 700 °C.

The lattice parameter *a* was determined from the XRD data for the powder calcined at 700 °C and found to be 7,39 Å. From the value of *a* and using equation (12), the theoretical density was found to be 5,056 g cm^{-3}.

To investigate the purity and composition of CCTO ceramics sintered at 1100 °C, EDS combined with Backscattered Electron Image (BEI) was performed. Figure 3.2 shows the presence of inclusions corresponding to the lighter regions and the main phase corresponding to the dark regions. The EDS analysis shows a very small variation of the ratio Cu/Ca (2,98) and Ti/Ca (3,97) from the stoichiometric relations (3 and 4, respectively) and, therefore, it is not possible to confirm what reactions are occurring in the ceramic. EDS is not an appropriate technique to determine very small variations in composition of a material and, therefore, the composition determined is within the detection limits of the equipment. However, the high relative amount of copper in the secondary phase, indicates the main phase to be Cu-deficient. In addition, zirconia is present in the CCTO main-phase and in the inclusion, resulting from contamination during milling

by the grinding media of Y_2O_3-stabilized ZrO_2. Yttrium was not detected probably because its content is too low and not detectable within the detection limits of the equipment.

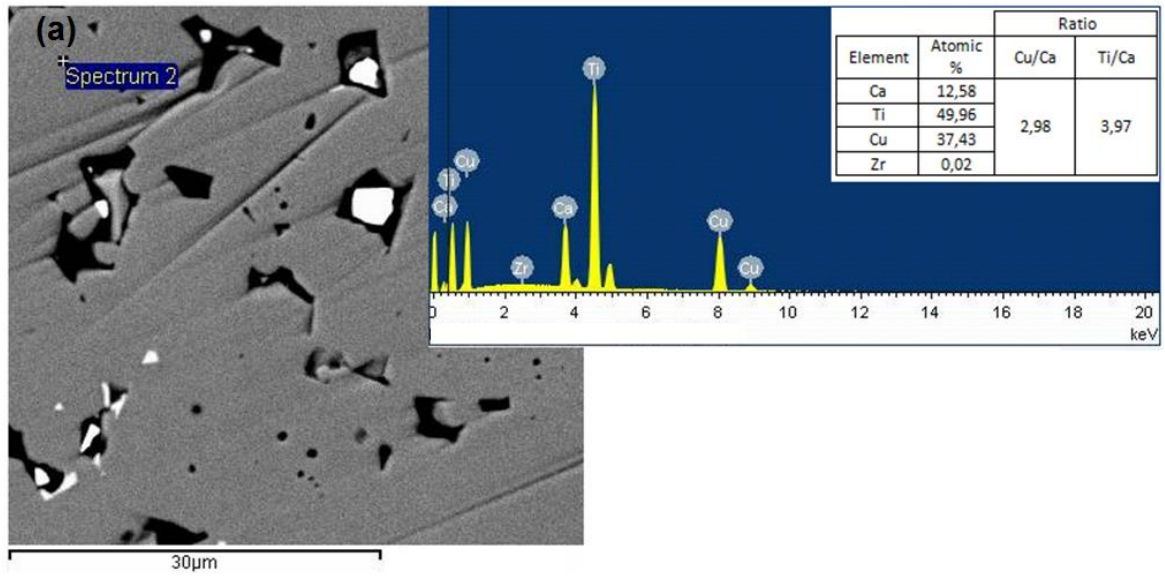

Element	Atomic %	Ratio Cu/Ca	Ratio Ti/Ca
Ca	12,58	2,98	3,97
Ti	49,96		
Cu	37,43		
Zr	0,02		

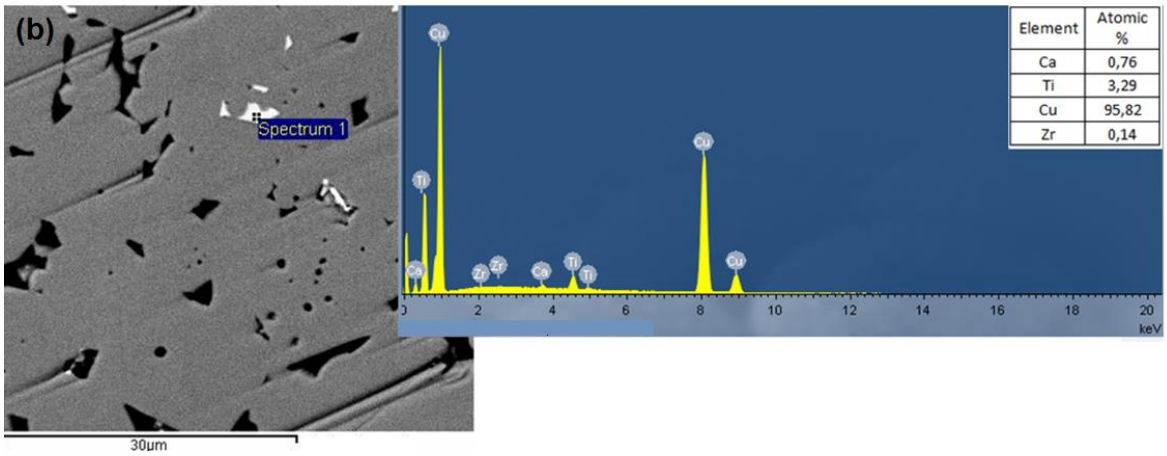

Element	Atomic %
Ca	0,76
Ti	3,29
Cu	95,82
Zr	0,14

Figure 3.2 – BEI and EDS of (a) main-phase and (b) inclusion of CCTO 1100 ceramics.

3.1.2. Electrical characterisation of CCTO ceramics

The electrical properties of CCTO ceramics were investigated using impedance spectroscopy. Sputtered Au electrodes were used for measurements performed at high temperatures and InGa (60:40) alloy paste electrodes for subambient measurements. Z* plots (Z” vs Z´) of CCTO samples

fired at 700, 800 and 900 ^{o}C are shown in figure 3.3 at 523 K. A single arc intercepting the origin of the Z'-axis is observed in all samples. In many electroceramics, each semicircular arc in these Z* plots can be modeled, to a first approximation, by an ideal parallel Resistor-Capacitor (RC) element and, hence, resistance R and capacitance C can be extracted by hand fitting of the semicircle. For CCTO 700 the resistivity and capacitance at 523 K are, respectively, 1,8 MΩ cm and 3,5 pF cm^{-1} (ε_r ~ 40), consistent with a bulk response, according to table 2. In comparison, CCTO 800 has a resistivity of 1,5 MΩ cm and capacitance of 4,2 pF cm^{-1} (ε_r ~ 50). Finally, CCTO 900 displays a resistivity of 4 MΩ cm and capacitance of 9,0 pF cm^{-1} (ε_r ~ 100), consistent with a bulk response. The relative densities for all these samples are very low, between 57 and 72 %, and, therefore, the high porosity has a small contribution for the high resistivity determined, once it constricts the current flow.

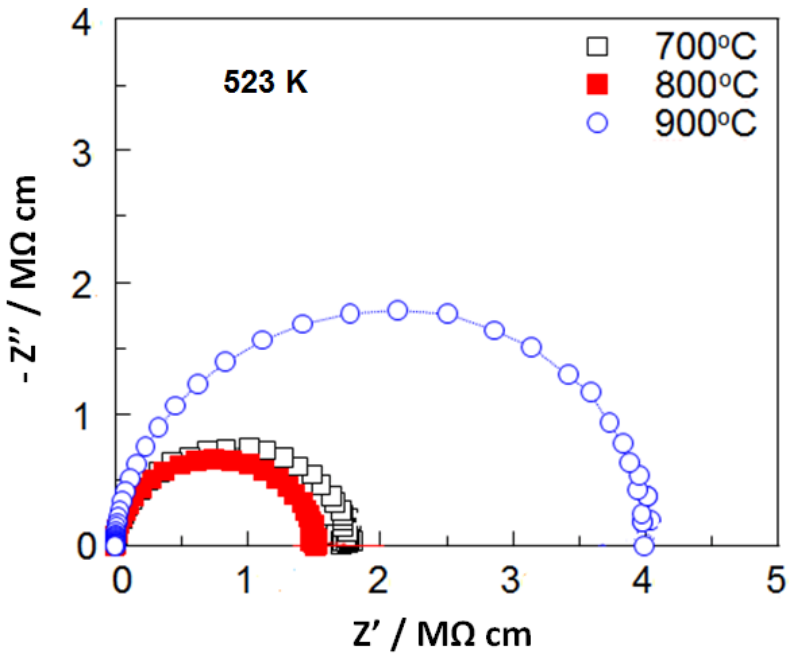

Figure 3.3 – Z* plots of CCTO 700, 800 and 900 ceramics at 523 K.

Figure 3.4 (a) shows the impedance complex plane, Z*, plots for CCTO 1000, at 523 K. In contrast with the previous samples, a non-zero intercept at high frequencies is observed, highlighted in the inset, indicating an additional response. The resistivity for the non-zero intercept is 40 Ω cm. The resistitivity and capacitance of the semicircle at intermediate frequencies are, respectively, ~ 530 Ω cm and ~ 2,0 nF cm^{-1} (ε_r ~ 19 000), consistent with a grain boundary response. The Z*

plots for CCTO 1100 is shown in figure 3.4 (b), at 523 K. A non-zero intercept is observed at high frequencies with a resistivity of ~ 30 Ω cm (inset of figure 3.4(b)). The arc resistivity and capacitance are ~ 65 kΩ cm and 1,1 nF cm^{-1} (ε_r ~ 12 500), consistent with a grain boundary response.

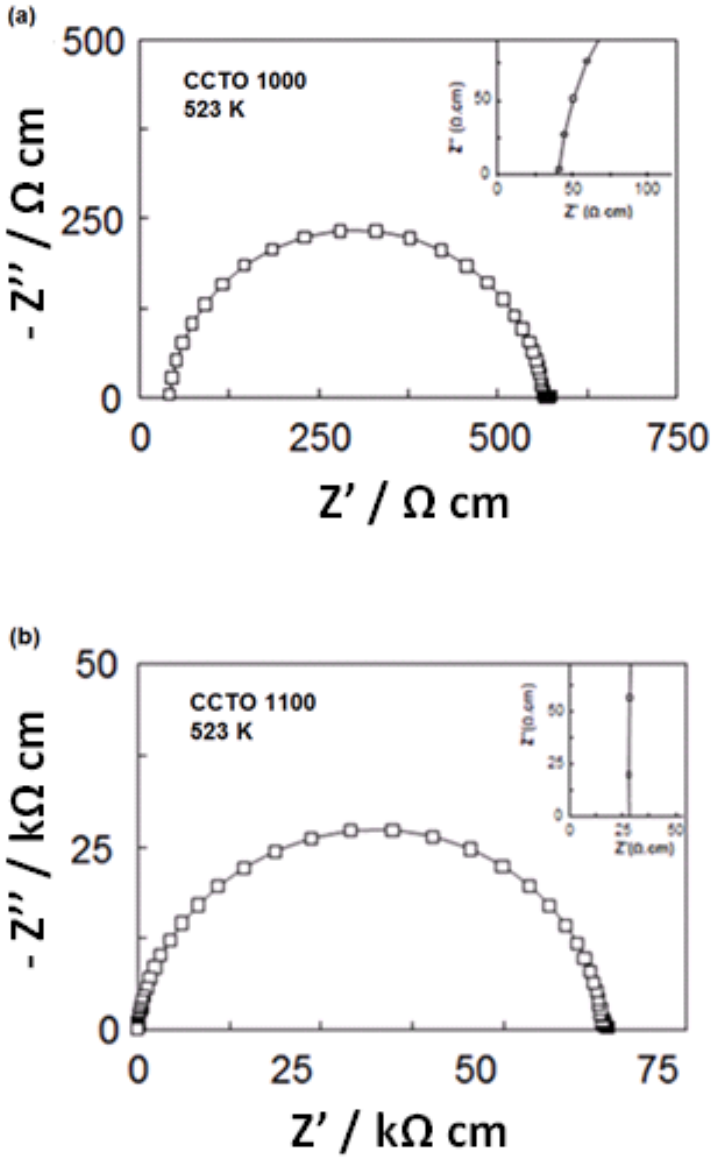

Figure 3.4 – Z* plots for (a) CCTO 1000 and (b) CCTO 1100 ceramics at 523 K.

Impedance spectra were also obtained under cryogenic conditions to get more information about the semiconducting response observed by the non-intercept at high frequencies in Z* plots of figure 3.4 (a) and (b), taking advantage of thermal activation to bring the relaxation frequencies

into the available experimental range. Z* plots at 80 K (figure 3.5) show one high frequency semicircle for both samples. The arc for CCTO 1000 has resistivity of ~ 250 kΩ cm and capacitance of ~ 11,0 pF cm^{-1} (ε_r ~ 125) and the arc for CCTO 1100 a resistivity of ~ 96 kΩ cm and capacitance of ~ 10,0 pF cm^{-1} (ε_r ~ 110), therefore, both are consistent with a bulk response. CCTO 1000 and 1100 can be, hence, modelled using the Brickwork Layer Model (BLM), as discussed in section 2.4.2.7, where a semiconducting bulk is consistent with a capacitance of ~ pF cm^{-1} and a grain boundary with a capacitance of ~ nF cm^{-1}.

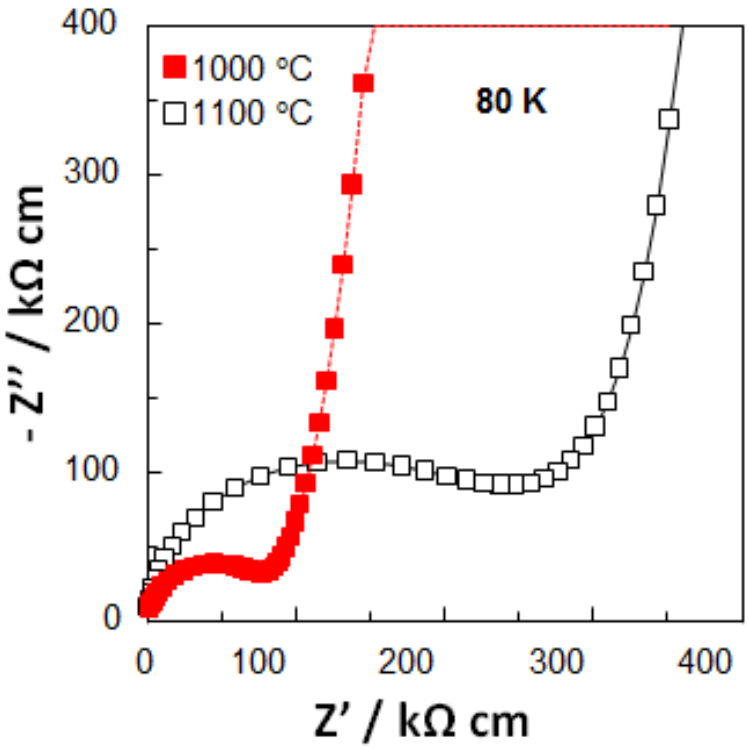

Figure 3.5 – Z* plots for CCTO 1000 and CCTO 1100 at 80 K.

Figure 3.6 shows the C spectroscopic plots at 523 K for all CCTO samples. For CCTO 1000 and 1100 two plateaux are observed: between low frequency and 10^6 Hz, a single plateau with high capacitance ~ nF cm^{-1} consistent with a grain boundary response and at high frequencies, > 10^6 Hz, a dispersion is observed, consistent with the presence of a semiconducting bulk response at higher frequencies. On the contrary, CCTO 700, 800 and 900 exhibit a single plateau over the complete frequency range with low capacitance of pF cm^{-1}, consistent with a bulk

response. The grain boundary response does not appear in the all temperature range as the samples have very low relative density, between 57 and 72 %, and therefore the microstructure consists only of grains.

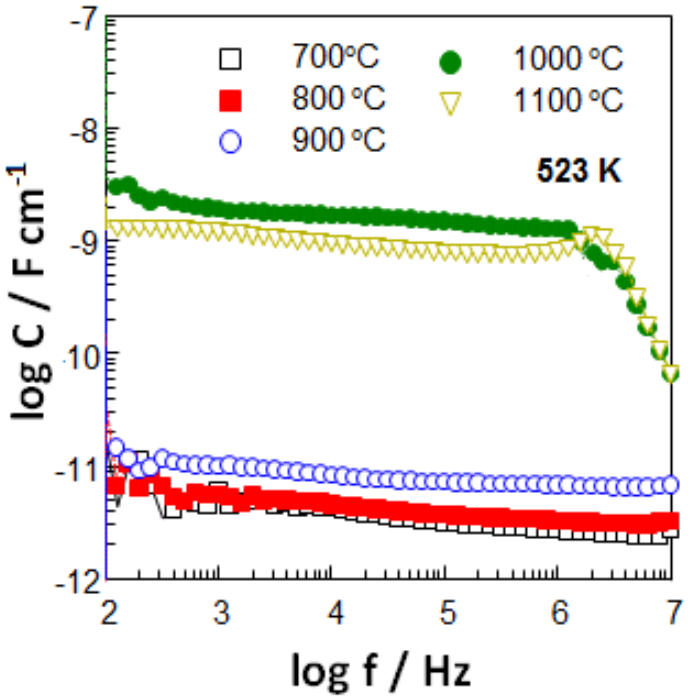

Figure 3.6 – C spectroscopic plots for all samples at 523 K.

Figure 3.7 shows the C spectroscopic plot at 10, 100 and 320 K for CCTO 1000 and 1100. The C spectroscopic plot at subambient temperatures helps to identify and characterise the other response observed at high frequencies in figure 3.4. Both samples show the same trend where at 320 K the high capacitance dominates almost all the frequency range.

At 100 K, both the low frequency grain boundary plateau and the high frequency bulk plateau are visible, with the dispersion moved to intermediate frequencies. At 10 K the plateau is totally dominated by the bulk as a low capacitance of ~ pF cm^{-1} is observed. Grain boundary capacitances, C_{gb}, of ~ 2,0 nF cm^{-1} and ~ 0,9 nf cm^{-1} for CCTO 1000 and 1100, respectively, were obtained from the low frequency plateau at 320 K, whereas the bulk capacitances, C_b of ~ 8,5 pF cm^{-1} for both samples were obtained from the high frequency plateau at 10 K.

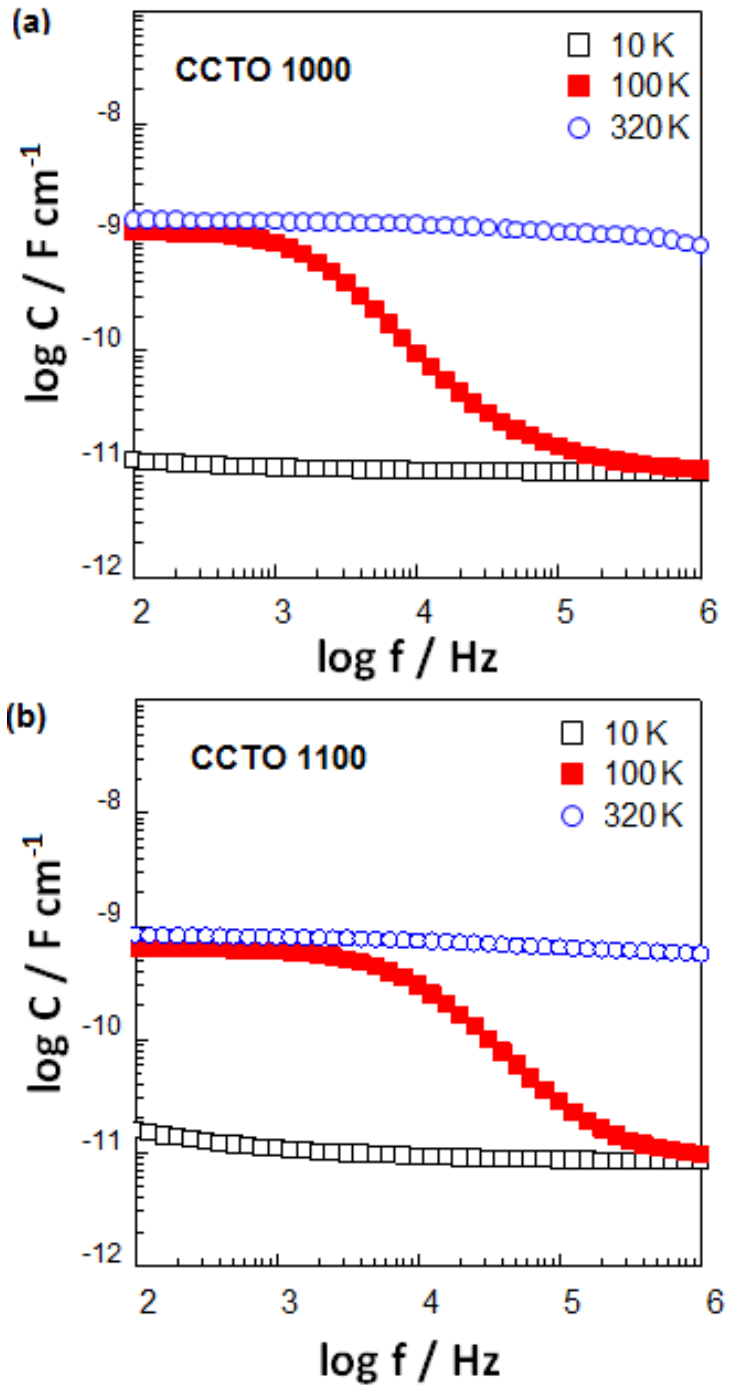

Figure 3.7 – C spectroscopic plots of (a) CCTO 1000 and (b) CCTO 1100 samples at 10, 100 and 320 K.

M'' spectroscopic plots for CCTO 700, 800 and 900 at subambient temperatures are shown in figure 3.8. M'', electric modulus, spectroscopic plots provide information sometimes not readily

available from Z* plots and permit to assess, in this case, the electrical homogeneity and temperature dependence of the bulk capacitance.

In IS, each parallel RC element results in a Debye peak in the M'' spectroscopic plot, where C is inversely to the double of M'' maximum peak, M''_{max}, corresponding to the Debye-peak. The Debye-peak is hence, dominated by the lowest capacitive component of a sample. CCTO 700 does not exhibit any Debye-peak at subambient temperatures, and therefore the bulk is totally resistive. The beginning of the peak at 320 K is due to a resistive grain response. However, when compared with CCTO 800 and 900 a Debye-peak is observed in all temperatures measured. In figure 3.8 (b) at 80 K, the presence of a Debye-peak at low frequencies, ~ 6 kHz, is observed and as the temperature increases, the Debye-peak shifts towards higher frequencies. At 260 K, this peak starts to disappear on the frequency window and another peak starts to appear at low frequencies, shifting to higher frequencies with increasing temperature. This indicates the bulk to consist in an inner semiconducting region surrounded by a resistive outer region. The first peak to disappear at high temperatures corresponds to the semiconducting region and the second peak to the resistive region. In figure 3.8 (c), the same trend is observed for CCTO 900 when compared with CCTO 800, indicating the bulk to be electrically heterogeneous as well.

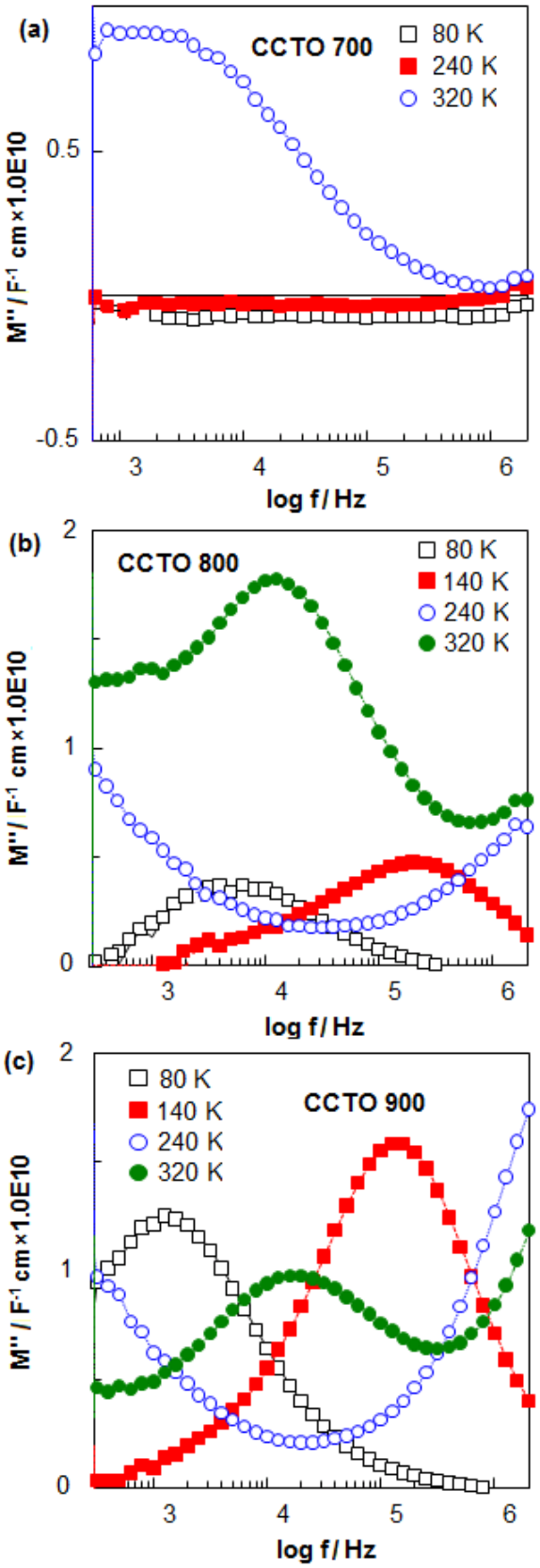

Figure 3.8 – M'' spectroscopic plots for (a) CCTO 700, (b) for CCTO 800 and (c) for CCTO 900 at subambient temperatures. The measurement temperatures are shown in the label.

The M'' spectroscopic plot of all samples is shown in figure 3.9, at 523 K. A large M'' peak is observed for CCTO 700, 800 and 900 with a maximum frequency similar for CCTO 700 and 800. For CCTO 900, M'' peak shifts towards lower frequencies. Using the equations $C=1/2M''_{max}$ and $R=1/w_{max}C$, at the maximum peak, the C and R values are respectively: 3,6 pF cm^{-1} and 1,1 MΩ cm for CCTO 700, 4,1 pf cm^{-1} and 1,6 MΩ cm for CCTO 800 and 8,3 pF cm^{-1} and 2,8 MΩ cm for CCTO 900. These results confirm samples to be consistent with the bulk response with values similar to those calculated from Z* plots, figure 3.3.

In contrast, the corresponding M'' spectra for CCTO 1000 and 1100 show a peak consistent with a grain boundary response [inset of figure 3.9] with capacitances of 1,4 nF cm^{-1} and 1,1 nf cm^{-1}, respectively, and resistivities of ~ 370 Ω cm and 47 kΩ cm. The additional high frequency incline in the M'' spectrum of CCTO 1000 and 1100 indicates a semiconducting bulk component with a time constant, τ, < 10^{-7} s. Therefore M''_{max} associated to the bulk response occurs at a frequency > 10^{7} Hz and, hence, not seen in the spectra. Lower temperature data is required to observe the M'' Debye-peak associated to the semiconducting bulk, figure 3.10.

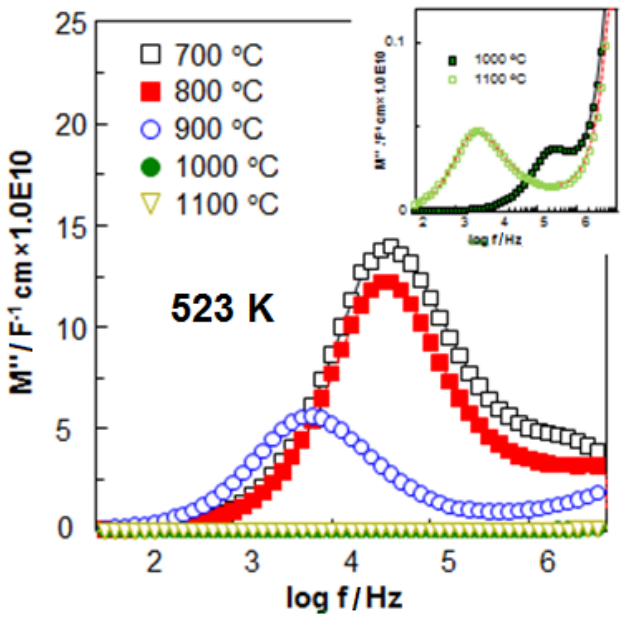

Figure 3.9 – M'' spectroscopic plot of CCTO for all samples at 523 K. An enlargement of the high capacitance region for CCTO 1000 and CCTO 1100 is shown in the inset.

Figure 3.10 shows the M'' spectroscopic plot for CCTO 1000 and 1100, at 80 K, where the bulk capacitance is similar for both samples as the M'' Debye-peak has the same height. The capacitance and resistivity calculated from M''_{max} peak gives values of ~ 10,0 nF cm^{-1} and 150 kΩ cm, respectively, for CCTO 1000. CCTO 1100 has a capacitance and resistivity of ~ 10,0 nF cm^{-1} and 62 kΩ cm, respectively. These values are close to those determined from Z* plots, at 80 K, figure 3.5. The M''_{max} peak for both samples appears at similar frequency, indicating the bulk composition and the intrinsic permittivity to be similar.

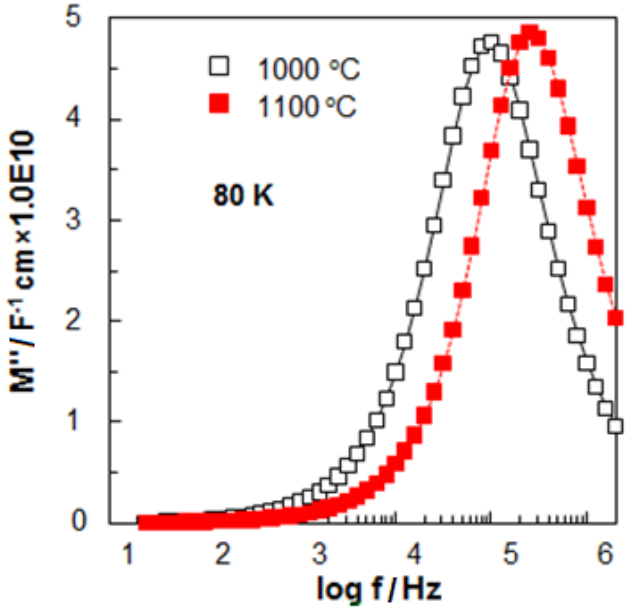

Figure 3.10 – M'' spectroscopic plot for CCTO 1000 and CCTO 1100 at 80 K.

The Arrhenius plot for bulk and grain boundary conductivities, σ_b and σ_{gb}, for all CCTO samples is shown in figure 3.11. The activation energy determined from the slope is shown in the label and phase 1 corresponds to the semiconducting bulk region and phase 2 to the resistive region. σ values were calculated using R values extracted from Z* plots and the relation σ=1/R. The conductivity determined at high temperatures follows linear Arrhenius-type behaviour, with activation energies between 0,78 and 0,93 eV for phase 2 of CCTO 700, 800 and 900 and grain boundary for CCTO 1000 and 1100.The bulk conductivity for CCTO 1000 and 1100 determined at subambient measurements displays slight non-Arrhenius behaviour, however, the activation energy was determined and found to be between 0,03 and 0,05 eV. Phase 1 of CCTO 800 and 900 follows approximately Arrhenius-type behaviour with activation energies between 0,07 and 0,08 eV.

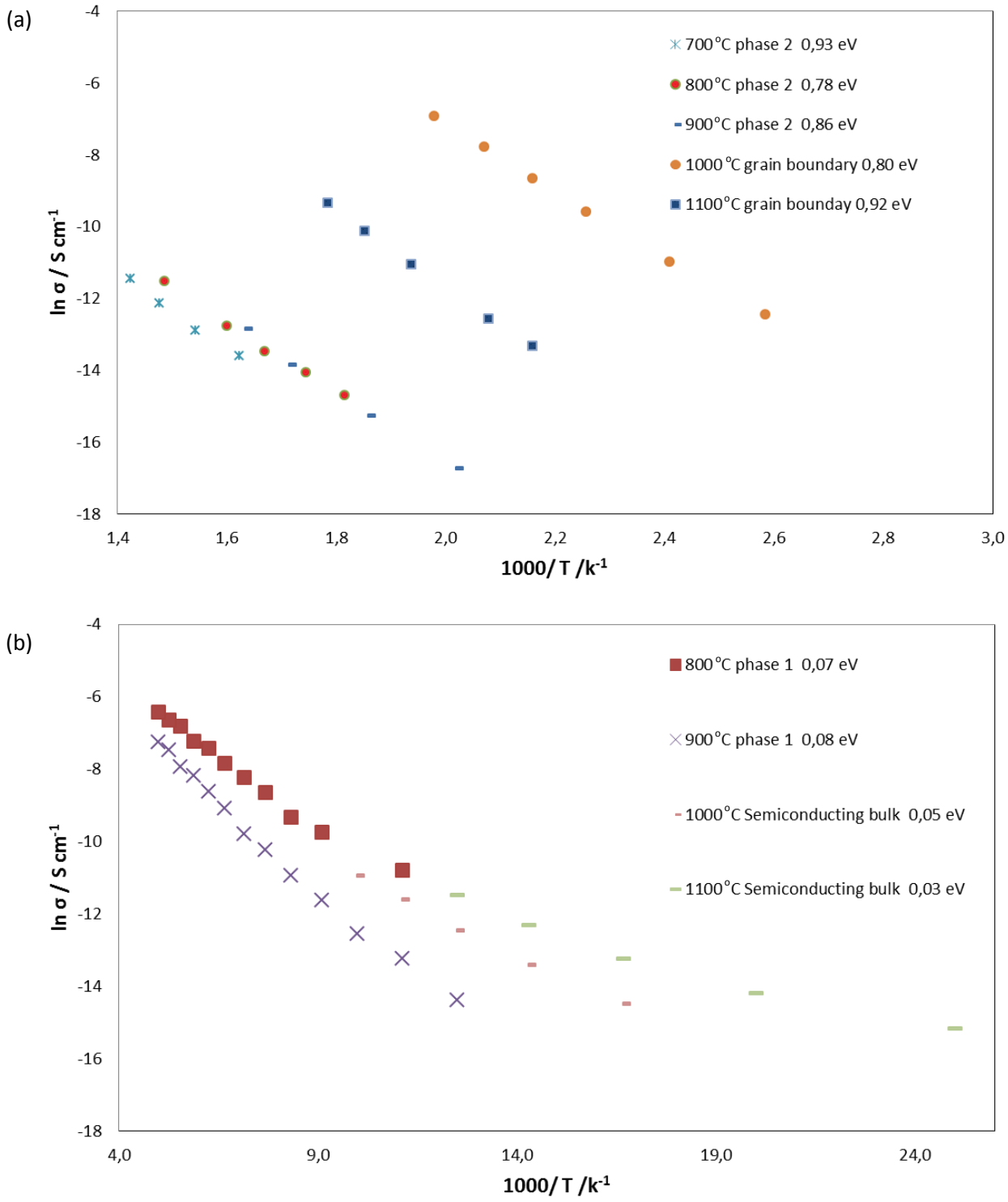

Figure 3.11 – Arrhenius plots comparing σ_b and σ_{gb} for all CCTO samples: (a) at high temperatures and (b) at low temperatures.

To assess the variation of composition of CCTO, the f_{max} plot is shown in figure 3.12. f_{max} corresponds to the frequency of the Debye-peak in the M'' spectroscopic plots and permits comparison of the composition between samples of the same material. Figure 3.12, shows the composition change for the bulk and grain boundary of CCTO ceramics. In the label, phase 1 is related to the semiconducting bulk region and phase 2 to the resistive bulk region. The curves related to the phase 2 for CCTO 700, 800 and 900 are overlaid, indicating the composition of the resistive bulk region to be similar. The composition for phase 1 of CCTO 800 and 900 is also similar. The semiconducting bulk for CCTO 1000 and 1100 is similar, however, different from the phase 1 for CCTO 800 and 900. In addition, the curve for the bulk of CCTO 1000 and 1100 shifts towards lower temperatures, indicating the bulk to become more conducting compared to the phase 1 of CCTO 800 and 900. The grain boundary composition changes from CCTO 1000 to CCTO 1100, where it becomes more resistive.

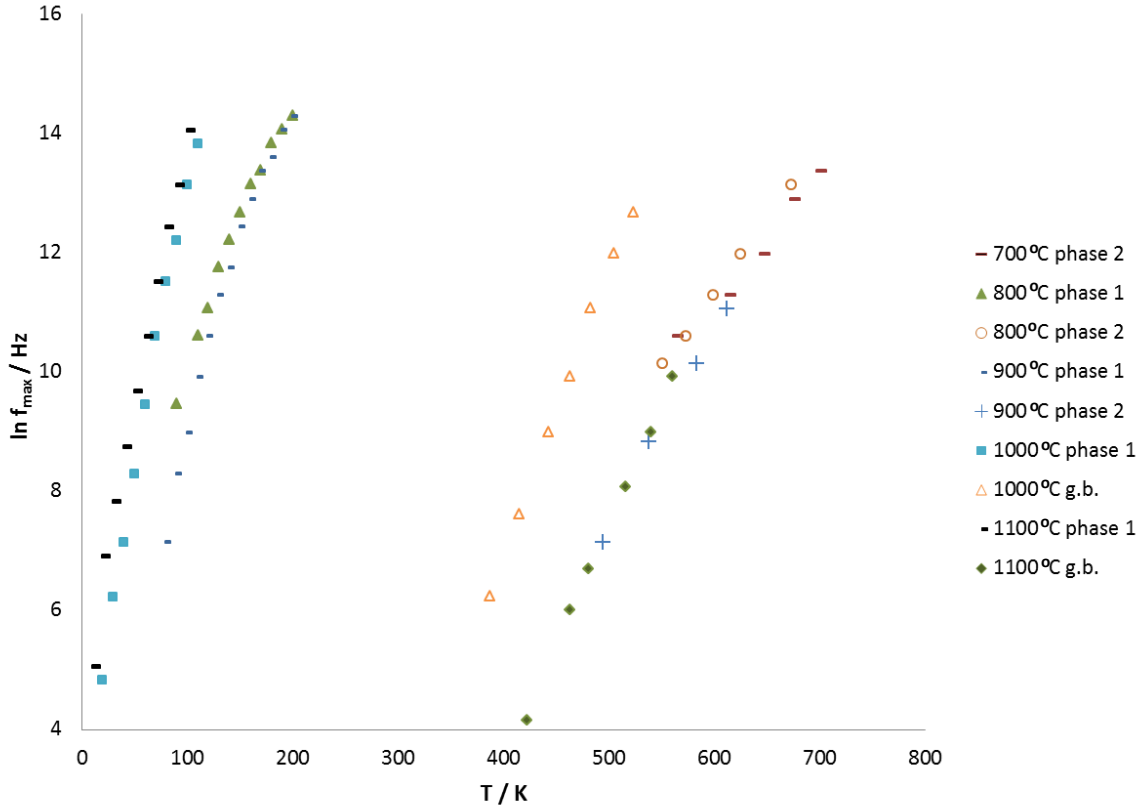

Figure 3.12 – Representation of the maximum frequency of M''_{max} peak with temperature for all samples.

Figure 3.13 shows the ratio between semiconducting and total phases (semiconducting + resistive regions) with sintering temperature. Phase 1 is related to the semiconductiong region and phase 2 to the resistive region (bulk and grain boundary regions). The relation was determined from M''_{max} values at 80 and 523 K, where the grain and grain boundaries responses can be extracted. It was considered, based on the data from impedance spectroscopy measurements, that both bulk and grain boundary capacitances are nearly independent of the measurement temperature. This means that any measurement temperature could be used and, therefore, 80 and 523 K were used since this document reports the electrical responses at these temperatures.

The semiconducting fraction increases as the sintering temperature increases, where for CCTO 1000 and 1100 the bulk is totally semiconducting. CCTO 700 does not appear in the figure as the bulk is totally resistive and, therefore, the relation used (in Y'-axis) cannot be applied in this situation.

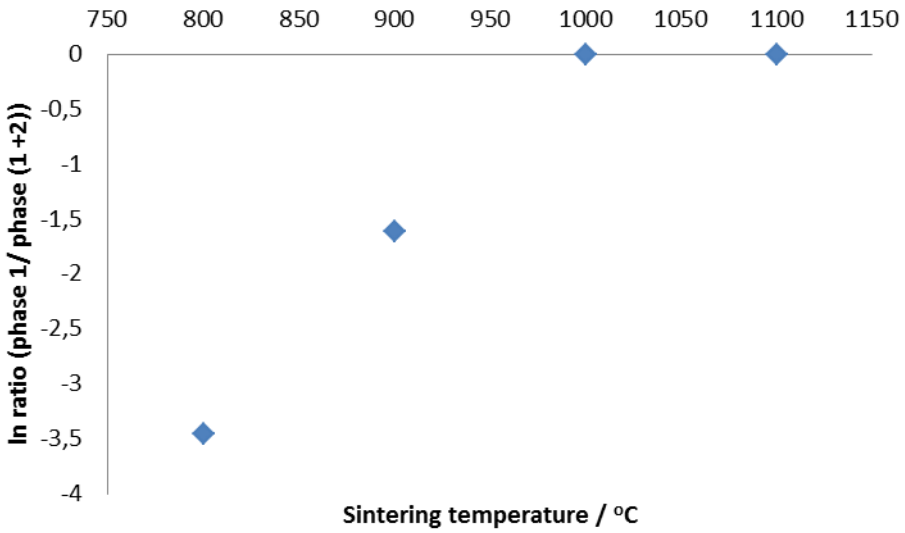

Figure 3.13 – Ratio between semiconducting and total phase (semiconducting + resistive phases) for samples sintered between 800 and 1100 ^{o}C.

Tables 4 and 5 show a summary of the main results obtained from this work. Table 4 shows the activation energy of the phase 1 (semiconducting phase) and phase 2 (resistive phase) and, the capacitance and resistivity of the samples obtained from Z'' vs Z' and M'' at 523 K. Table 5 shows the capacitance and resistivity of the samples extracted from Z'' vs Z' and M'', at 80 K, and the ratio between the semiconducting phase (phase 1) and total phase.

Table 4 – Summary of the results for the activation energy, and resistivity and capacitance extracted from Z'' vs Z' and M'' plots at 523 K.

Phase 1 is related to the semiconducting region and phase 2 to the resistive region (resistive bulk and grain boundary regions).

		High temperature (**523 K**)				
		Z'' vs Z'		**M''**		
Sample	Activaction energy (eV)	**R** (Ω cm)	**C** (pF cm^{-1})	**M''$_{max}$** (F^{-1} cm)	**C** (pF cm^{-1})	**R** (Ω cm)
CCTO 700	phase **1** : -----	$1{,}8 \times 10^6$	3,5	14×10^{10}	3,6	$1{,}1 \times 10^6$
	phase **2** : 0,93					
CCTO 800	phase **1** : 0,07	$1{,}5 \times 10^6$	4,2	12×10^{10}	4,1	$1{,}6 \times 10^6$
	phase **2** : 0,78					
CCTO 900	phase **1** : 0,08	$4{,}0 \times 10^6$	9,0	$5{,}6 \times 10^{10}$	8,3	$2{,}8 \times 10^6$
	phase **2** : 0,86					
CCTO 1000	phase **1** : 0,05	530	$2{,}0 \times 10^3$	$3{,}6 \times 10^8$	$1{,}4 \times 10^3$	370
	phase **2** : 0,80					
CCTO 1100	phase **1** : 0,03	65×10^3	$1{,}1 \times 10^3$	$3{,}7 \times 10^8$	$1{,}0 \times 10^3$	47×10^3
	phase **2** : 0,92					

Table 5 – Summary of the results for the capacitance and resistivity, at 80 K, extracted from Z'' vs Z' and M'' plots. The table also provides the ratio between the semiconducting and total phases.

	Low temperature (**80 K**)					
	Z'' vs Z'		**M''**			
Sample	**R** (Ω cm)	**C** (pF cm^{-1})	**M''$_{max}$** (F^{-1} cm)	**C** (pF cm^{-1})	**R** (Ω cm)	**M''$_{max}$ ratio phase 1 / (phases (1+2))**
CCTO 700	---	---	---	---	---	0,00
CCTO 800	---	---	$3{,}8 \times 10^9$	130,0	$9{,}7 \times 10^4$	0,03
CCTO 900	---	---	12×10^9	41,6	300×10^4	0,20
CCTO 1000	250×10^3	11,0	47×10^9	10,5	152×10^3	0,99
CCTO 1100	96×10^3	10,0	48×10^9	10,3	62×10^3	0,99

3.2. Discussion

Powders were shown to be single phase CCTO, by X-ray diffraction, when calcined at 700 ^{o}C, indicating the high-energy ball milling to be successful in the production of single-phase CCTO at lower temperatures when compared to the conventional solid state reaction (950 - 1100 ^{o}C). At the calcination temperature of 650 ^{o}C, secondary phases are still present.

A secondary phase was detected in ceramics sintered at 1100 ^{o}C and the chemical analysis showed this phase to be Cu-rich and, therefore, the main phase is Cu-deficient. This change in the composition of CCTO ceramics contributes to the increase of the bulk semiconductivity. The detection of zirconia in the CCTO phase resulted from the contamination of the grinding media used during milling and it may also affects the electrical properties of CCTO ceramics.

CCTO 700 ceramics exhibit resistive bulk with resistivity of ~ 1,8 MΩ cm at 523 K obtained from Z* plots and confirmed by M'' spectroscopic plot (fig. 3.3) by the absence of any Debye-peak at subambient temperatures. The capacitance of ~ 3,5 pF cm^{-1} confirms the response to be due to the bulk region. Contrary to what is reported in the literature for CCTO ceramics, an IBLC electrical microstructure is not present as the bulk is resistive and a single plateau is observed in the C spectroscopic plot, figure 3.6. CCTO 700 behaves as an insulator and the ceramic has low relative density, 57 %.

CCTO 800 and 900 also exhibit, in Z* plots at 523 K, (figure 3.3) an absence of a non-zero intercept in Z´-axis, suggesting the bulk to be resistive. The bulk resistivity, at 523 K, for these two samples are 1,5 and 4 MΩ cm and the capacitance 3,2 and 9,0 pF cm^{-1}, respectively. The C plateau in figure 3.6 also confirms the data to be related to the bulk response. However, M'' spectroscopic plots, figure 3.8 (a), for CCTO 800 show at 260 K two Debye-peaks: the high frequency peak corresponds to a semiconducting bulk region and the low frequency is related to a resistive bulk region. This indicates the bulk to be electrically heterogeneous consisting in an inner semiconducting core surrounded by a resistive region. The same trend can be observed for CCTO 900 and the ratio between semiconducting and total region (figure 3.13) of the bulk increases with the sintering temperature.

In contrast, CCTO 1000 and CCTO 1100 display an IBLC microstructure, similar to that of CCTO ceramics found in the literature. Using IS, the grain boundary resistivity, at 523 K, is ~ 530 Ω cm

and bulk resistivity ~ 40 Ω cm for CCTO 1000. For CCTO 1100, the grain boundary and bulk resistivity are, respectively, ~ 65 kΩ cm and ~ 30 Ω cm. Comparing CCTO 1000 and 1100, the bulk resistivity is similar, however, a substantial difference is seen for the grain boundary resistivity: CCTO 1100 grain boundary resistivity is almost 2 orders of magnitude greater than CCTO 1000. This may be attributed to the presence of a reoxidized grain boundary composition favored at higher temperatures of sintering. The ratio between semiconducting and total phase of the bulk, figure 3.13, confirms the bulk to be totally semiconducting. To confirm the non-intercept response in Z'-axis of Z* plots for CCTO 1000 and 1100, an additional Z* plots at lower temperature, at 80 K, is shown in figure 3.5, where the capacitance of ~ 10,0 pF cm^{-1} for both samples confirms that the low resistivity at high frequencies observed in Z* plots at 523 K is related to the bulk component. The IBLC mechanism starts to emerge, therefore, at the sintering temperature of 800 ^{o}C and increases as the sintering temperature increases.

In the Z* plots at 80 K, R_b is ~ 250 and 96 kΩ cm for CCTO 1000 and CCTO 1100, respectively. Analysis of the Z* plots for these two samples at low temperatures is required, where the resistivity of the semiconducting bulk becomes high enough to be observable within the frequency range of measurement, Hz - MHz, and the electrical response characterised.

The σ_b and σ_{gb} for all samples is shown in Arrhenius plot format in figure 3.11. σ_b of sample CCTO 700 and phase 2 (resistive region) of CCTO 800 and 900 is very similar and follows linear Arrhenius- type behaviour. The activation energy is between 0,78 and 0,93 eV, suggesting similar bulk composition. On the other hand, the activation energy is similar to that observed for the grain boundary for CCTO 1000 and 1100, indicating the mechanism of conduction to be similar. σ_{gb} of CCTO 1000 and 1100 are higher compared with the resistive bulk of CCTO 700, 800 and 900. CCTO 1000 σ_{gb} is higher compared to CCTO 1100, which is in accordance with Z* plots at 523 K, figure 3.4.

The bulk conductivity of phase 1 in CCTO 800, CCTO 900, CCTO 1000 and CCTO 1100, measured at subambient temperatures, displays slight non-Arrhenius behaviour and, therefore, the activation energy determined is not so accurate. However, the bulk of CCTO 1100 is more conducting than CCTO 1000, showing that higher sintering temperatures contribute to a higher decomposition of the CCTO bulk ceramics.

The C spectroscopic plot, figure 3.6, shows for CCTO 700, 800 and 900, a single and frequency independent plateau response. The capacitances obtained from C spectroscopic plot are, respectively, 4,0 pF cm^{-1} for both CCTO 700 and 800, and 9,0 pF cm^{-1} for CCTO 900, giving values

of permittivity approximately 40 and 110, consistent with the values obtained from Z* plots. In contrast with the results available in the literature, the 'giant' permittivity for undoped CCTO does not appear in these samples.

For CCTO 1000 and 1100, the high capacitance at low frequencies is consistent with a grain boundary response and, at high frequencies, the dispersion of capacitance is related to the semiconducting bulk and this is in accordance with the information displayed in the literature, where two different responses are observed in C spectroscopic plots. Although and as mentioned before in section 2.4.2.7., it is not possible to calculate accurately the capacitance of the grain boundary, however, from the low frequency plateau is possible to determine the gb capacitances of 2 and 1 nF cm^{-1}, giving rise to the permittivities of ~ 18 000 and 11 300, for CCTO 1000 and 1100. The 'giant' permittivity appears, therefore, for CCTO 1000 and 1100 samples and, it seems associated with the presence of a thin and reoxidized grain boundary region on the outer surfaces of the semiconducting grain.

Interestingly, CCTO 1000 capacitance is higher compared to that of CCTO 1100 sample. According to equation (4), larger grains result in higher effective permittivity whereas the grain boundary thickness and intrinsic permittivity are usually assumed to be constant. According to the fundaments of sintering, when the sintering temperature rises, it usually gives rise to larger grains and, therefore, it would be expected the effective permittivity of CCTO 1100 to be higher. The justification should, therefore, focus on the effective permittivity and/or grain boundary which may change with the processing conditions.

4. Conclusion

Pure phase $CaCu_3Ti_4O_{12}$ was synthesized at lower temperature by high-energy ball milling. X-ray diffraction revealed that pure phase CCTO powders can be obtained on calcination at 700 ^oC for 12 hours. At the calcination temperature of 650 ^oC, the presence of secondary phases of TiO_2 and CuO are observed on XRD data.

From the microstructure study on CCTO 1100 sample, the main-phase is Cu-deficient and this contributed towards the increasing of the bulk conductivity in CCTO. However, the mechanism responsible for the origin of the bulk semiconductivity is not well understood yet, but it may be associated to the diffusion and eventual volatililisation of copper at elevated temperatures of processing.

Impedance spectroscopy measurements showed different electrical microstructures for the sintered pellets. CCTO 700 is an insulator with low relative density (57 %) and with a bulk resistivity > 1 MΩ cm. CCTO 800 and 900 are composed of semiconducting inner grains surrounded by insulating outer grain regions. The grains have become totally semiconducting when the sintering temperature increased to 1000 ^oC. IS results show, therefore, a general picture about the evolution of the IBLC mechanism in CCTO ceramics with sintering temperature where the conducting phase emerges and grows from the core part of grains at the expense of phase R. The conducting phase exhibits resistivity < 100 Ω cm, at 523 K. The volume fraction of resistive phase in the grains decrease until it becomes a resistive thin layer corresponding to the grain boundary region, for samples sintered at 1100 ^oC. The change in the resistivity of the phases seems to be influenced by Cu-loss mechanism that may diffuse within grains towards grain boundaries at elevated temperatures. The resistive phase CCTO can be prepared at low temperatures by high-energy ball milling where the Cu-loss mechanism is suppressed as shown by the absence of any peak in M'' spectroscopic plot for samples sintered at 700 ^oC. However, the high temperature required to get dense CCTO ceramics promotes the Cu-loss and, therefore, the grains become semiconducting. The IBLC mechanism starts to appear when the sintering temperature reaches 800 ^oC and its effect gets higher as the sintering temperature increases and it is responsible for the 'giant' permittivity observed for CCTO 1000 and 1100, where the bulk is completely semiconducting.

5. Future Work

To date there have been no transport studies on low temperature sintered CCTO ceramics that primarily consist of insulating phase and therefore the type of charge carrier in it is unknow. The conduction mechanisms in insulating phase and even in semiconducting phase remain unclear at this stage. Further studies on the pO_2 dependence of the conductivity of insulating phase in ceramics in combination with Thermoelectric power measurements, Transmission Electron Microscopy (TEM) and Electron Energy Loss spectroscopy (EELS) measurements need to be done to resolve the conduction mechanisms in CCTO ceramics.

References

1. Cross, L. E., Newnham, R. E. History of Ferroelectrics. Journal of the American Ceramic Society, **111,** 1987.

2. Wang, H. L. Structure and Dielectric Properties of Perovskite. University of San Jose State, 2002.

3. Homes, C. C., Vogt, T., Shapiro, S. M., Wakimoto, S., Ramirez, A. P. Optical response of high-dielectric-constant perovskite-related oxide. Science (New York), **293**, 673, 2001.

4. Subramanian, M. A., Li, D., Duan, N., Reiner, B. A., Sleight, A. W. High Dielectric Constant in $ACu_3Ti_4O_{12}$ and $ACu_3Ti_3FeO_{12}$ Phases. Solid State Chemistry, **151**, 323–325, 2000.

5. Ramirez, A. P., Subramanian, M. A., Gardel, M., Blumberg, M., Li, D., Vogt, T., Shapiro, S. M. Giant dielectric constant response in a copper-titanate. Solid State Communications, **115**, 217–220, 2000.

6. Wang, C. M., Kao, K. S., Lin, S. Y., Chen, Y. C., Weng, S.C. Processing and properties of $CaCu_3Ti_4O_{12}$ ceramics. Physics and Chemistry of Solids, **69**, 608–610, 2008.

7. Ezhilvalavan, S., Tseng, T. Y. Progress in the developments of $(Ba,Sr)TiO_3$ (BST) thin films for Gigabit era DRAMs. Materials Chemistry and Physics, **65**, 227–248, 2000.

8. Woodward, P. M. Octahedral Tilting in Perovskites - Geometrical Considerations. Acta Crystallographica B, **53**, 32–43, 1997.

9. Johnsson, M., Lemmens, P. Crystallography and Chemistry of Perovskites. University of Stockholm, 2005.

10. Howard, C. J., Stokes, H. T. Structures and phase transitions in perovskites - a group-theoretical approach. Acta Crystallographica A, **61**, 93–111, 2005.

11. Howard, C. J., Stokes, H. T. Group-Theoretical Analysis of Octahedral Tilting in Perovskites. Acta Crystallographica B, **54**, 782-789, 1998.

12. Zhou, J.S., Goodenough, J. B. Intrinsic structural distortion in orthorhombic perovskite oxides. Physical Review B, **77**, 2–5, 2008.

13. Fierro, J. L. G., Pena, M.A. Chemical Structures and Performance of Perovskite Oxides. American Chemical Society, **101**, 1981-2017, 2001.

14. King, G., Woodward, P. M. Cation ordering in perovskites. Materials Chemistry, **20**, 5785–5796, 2010.

15. Bozin, E.S., Petkov, V., Barnes, P.W., Woodward, P.M., Vogt, T., Mahanti, S.D., Billinge, S.J.L.Temperature dependent total scattering structural study of $CaCu_3Ti_4O_{12}$. Journal of Physics: Condensed Matter, **16**, 5091-5102, 2004.

16. Barnes, P. W., Lufaso, M. W., Woodward, P. M. Structure determination of $A_2M^{3+}TaO_6$ and $A_2M^{3+}NbO_6$ ordered perovskites: octahedral tilting and pseudosymmetry. Acta Crystallographica, **62**, 384–396, 2006.

17. Subramanian, M. A., Sleight, A. W. $ACu_3Ti_4O_{12}$ and $ACu_3Ru_4O_{12}$ perovskites : high dielectric constants and valence degeneracy. Solid State Sciences, **4**, 347–351, 2002.

18. Yuan, W. Investigation on the decomposable process and the secondary liquid phase effect on the dielectric properties of $CaCu_3Ti_4O_{12}$ ceramics. Physics D: Applied Physics, **42**, 175401, 2009.

19. Ferrarelli, M. C., Sinclair, D. C., West, A. R. Structure-Composition-Property Relations in the $ACu_3Ti_4O_{12}$ Structure-type. University of Sheffield, 2008.

20. Vijatović, M. M., Bobić, J. D., Stojanović, B. D. History and Challenges of Barium Titanate: Part II. Science of Sintering, **40**, 235–244, 2008.

21. Vijatović, M. M., Bobić, J. D., Stojanović, B. D. History and Challenges of Barium Titanate : Part I. Science of Sintering, **40**, 155–165, 2008.

22. Callister, W.D. Materials Science and engineering An Introduction, 7th edition, 2006.

23. He, L., Neaton, J.B., Cohen, M. H. Vanderbilt, D. A first-principles study of the structure and lattice dielectric response of $CaCu_3Ti_4O_{12}$. Physics Review B, **65**, 214112, 2002.

24. Leroy, W. A fundamental study of advanced metal / semiconductor contacts. University of Wetenschappen, 2007.

25. Moulson, A.J., Herber, J.M. Electroceramics. 2th edition, 2003.

26. Lunkenheimer, P., Fichtl, R., Ebbinghaus, S. G., Loidl, A. Non-intrinsic origin of the Colossal Dielectric Constants in $CaCu_3Ti_4O_{12}$. Physics Review, **1**, 19–22, 2004.

27. Adams, B. T. B., Sinclair, D. C., West, A. R. Giant Barrier Layer Capacitance Effects in $CaCu_3Ti_4O_{12}$ Ceramics. Advanced Materials, **14**, 2001–2003, 2002.

28. Adams, T. B., Sinclair, D. C., West, A. R. Influence of Processing Conditions on the Electrical Properties of $CaCu_3Ti_4O_{12}$ Ceramics. Journal of the American Ceramic Society, **89**, 3129–3135, 2006.

29. Sinclair, D. C., Adams, T. B., Morrison, F. D., West, A. R. $CaCu_3Ti_4O_{12}$: One-step internal barrier layer capacitor. Applied Physics Letters, **80**, 2153, 2002.

30. Kim, I.D., Rothschild, A., Tuller, H. L. Direct current bias effects on grain boundary Schottky barriers in $CaCu_3Ti_4O_{12}$. Applied Physics Letters, **88**, 072902, 2006.

31. Chung, S. Y., Kim, I.D., Kang, S. J. L. Strong nonlinear current-voltage behaviour in perovskite-derivative calcium copper titanate. Nature Materials, **3**, 774–778, 2004.

32. Li, M., Feteira, A., Sinclair, D. C., West, A. R. Influence of Mn doping on the semiconducting properties of $CaCu_3Ti_4O_{12}$ ceramics. Applied Physics Letters, **88**, 232903, 2006.

33. Belous, A., Ovchar, O., Valant, M., Krzmanc, M. Suvorov, D. Microwave composite dielectrics based on magnesium titanates. Journal of European Ceramic Society, **27**, 2963–2966, 2007.

34. Bender, B. A., Pan, M. J. The effect of processing on the giant dielectric properties of $CaCu_3Ti_4O_{12}$. Materials Science and Engineering, **117**, 339–347, 2005.

35. Yang, J., Shen, M., Fang, L. The electrode/sample contact effects on the dielectric properties of the $CaCu_3Ti_4O_{12}$ ceramic. Materials Letters, **59**, 3990–3993, 2005.

36. Patterson, E. A., Kwon, S., Huang, C., Cann, D. P., Patterson, E. A. Effects of ZrO_2 additions on the dielectric properties of $CaCu_3Ti_4O_{12}$. Applied Physics Letters, **182911**, 10–13, 2005.

37. Feng, L., Tang, X., Yan, Y., Chen, X., Jiao, Z., Cao, G. Decrease of dielectric loss in $CaCu_3Ti_4O_{12}$ ceramics by La doping. Physics State Solids, **4**, 22–24, 2006.

38. Varma, B. S. R., Prakash, B. S. Microstructural and dielectric properties of donor doped (La^{3+}) $CaCu_3Ti_4O_{12}$ ceramics. Materials Science, **17**, 899–907, 2006.

39. Chen, Y., Li, C. P., Chen, H., Chen, Y. One-dimensional nanomaterials synthesized using high-energy ball milling and annealing process. Science and Technology of Advanced Materials, **7**, 839–846, 2006.

40. West, A. R., Sinclair, D. C., Hirose, N. Characterization of Electrical Materials, Especially Ferroelectrics by Impedance Spectroscopy. Electroceramics, **1:1**, 65–71, 1997.

41. Sinclair, D. C. Characterization of Electro-materials using ac Impedance Spectroscopy. Cerámica y Vidrio**, 34**, 55–66, 1995.

42. Macdonald, J.R. Impedance Spectroscopy. Annals of Biomedical Engineering, **20**, 289–305, 1992.

43. Irvine, J. T. S., Sinclair, D. C., West, A. R. Electroceramics: Characterization by Impedance Spectroscopy. Advanced Materials, **2**, 132–138, 1990.

44. Fleig, J. The influence of non-ideal microstructures on the analysis of grain boundary impedances. Solid State Ionics, **131**, 117–127, 2000.

45. Fleig, J., Maier, J. The impedance of ceramics with highly resistive grain boundaries: validity and limits of the brick layer model. Journal of European Ceramic Society, **19**, 693–696, 1999.